APL Materials

Control of spin–charge conversion in van der Waals heterostructures

Cite as: APL Mater. **9**, 100901 (2021); https://doi.org/10.1063/5.0054865
Submitted: 22 April 2021 • Accepted: 06 July 2021 • Published Online: 12 October 2021

Regina Galceran, Bo Tian, Junzhu Li, et al.

Control of spin–charge conversion in van der Waals heterostructures

Cite as: APL Mater. 9, 100901 (2021); doi: 10.1063/5.0054865
Submitted: 22 April 2021 • Accepted: 6 July 2021 •
Published Online: 12 October 2021

Regina Galceran,[1] Bo Tian,[2] Junzhu Li,[2] Frédéric Bonell,[3] Matthieu Jamet,[3] Céline Vergnaud,[3] Alain Marty,[3] Jose H. García,[1] Juan F. Sierra,[1] Marius V. Costache,[1] Stephan Roche,[1,4] Sergio O. Valenzuela,[1,4] Aurélien Manchon,[5] Xixiang Zhang,[2] and Udo Schwingenschlögl[2,a)]

AFFILIATIONS

[1] Catalan Institute of Nanoscience and Nanotechnology (ICN2), CSIC and BIST, Campus UAB, Bellaterra, 08193 Barcelona, Spain
[2] King Abdullah University of Science and Technology (KAUST), Physical Science and Engineering (PSE), Thuwal 23955-6900, Saudi Arabia
[3] University of Grenoble Alpes, CNRS, CEA, Spintec, 38000 Grenoble, France
[4] ICREA–Institució Catalana de Recerca i Estudis Avançats, 08010 Barcelona, Spain
[5] Aix-Marseille Université, CNRS, CINaM, Marseille, France

Note: This paper is part of the Special Topic on Emerging Materials for Spin-Charge Interconversion.
[a)] **Author to whom correspondence should be addressed:** udo.schwingenschlogl@kaust.edu.sa

ABSTRACT

The interconversion between spin and charge degrees of freedom offers incredible potential for spintronic devices, opening routes for spin injection, detection, and manipulation alternative to the use of ferromagnets. The understanding and control of such interconversion mechanisms, which rely on spin–orbit coupling, is therefore an exciting prospect. The emergence of van der Waals materials possessing large spin–orbit coupling (such as transition metal dichalcogenides or topological insulators) and/or recently discovered van der Waals layered ferromagnets further extends the possibility of spin-to-charge interconversion to ultrathin spintronic devices. Additionally, they offer abundant room for progress in discovering and analyzing novel spin–charge interconversion phenomena. Modifying the properties of van der Waals materials through proximity effects is an added degree of tunability also under exploration. This Perspective discusses the recent advances toward spin-to-charge interconversion in van der Waals materials. It highlights scientific developments which include techniques for large-scale growth, device physics, and theoretical aspects.

I. INTRODUCTION

In the search for continued miniaturization of microelectronic devices, two-dimensional (2D) materials, such as graphene and its siblings, offer opportunities to radically change the technology landscape by enabling the discovery of revolutionary device paradigms.[1,2] Although the path to technological implementation is long and hard, the extraordinary burst of 2D material synthesis during the last decade allowed for the fabrication of a wide variety of 2D materials,[1,3] opening thrilling avenues for the design of innovative atomically flat devices. 2D materials possess strong covalent bonds between atoms in the plane, but their out-of-plane interaction is mediated by 1000 times weaker van der Waals (vdW) forces, which enables an easy delamination of these layered materials. The interfaces obtained are defect-free and extremely sensitive to their environment.[4] This offers a unique playground of study, as the properties of one material can be transferred to its neighbor by proximity effects when stacking different materials in complex vdW heterostructures. While the device performance is yet to challenge the existing traditional technology,[5] their ability for unconventional operation nurtures the search for innovative concepts, such as the inclusion of the spin, pseudospin, and valley degrees of freedom.[6,7]

To address the issues related to the energy loss in devices (e.g., gate leakages, interconnects, and refreshing non-volatile

memories), spin angular momentum can be used to store, transmit, and manipulate information with high efficiency in terms of energy consumption.[2,8–11] In fact, highly efficient spin transport[12–14] and long spin diffusion[15–21] can be achieved in graphene and transition metal dichalcogenides (TMDs),[22,23] enabling the fabrication of spin-field effect transistors[24–26] and novel spin filtering devices.[27,28] However, traditional spin-devices require spin injection from magnetic elements, usually made of transition metal materials such as NiFe or CoFe, and the application of magnetic fields to define their magnetization orientation. This is a challenge because good interface quality between the ferromagnet (FM) and the 2D vdW substrate is of critical importance and difficult to achieve.[12,13,29] Furthermore, the use of magnetic fields to switch the magnetization limits the density of magnetic elements. These limitations severely hindered the performance of flat spintronic devices despite the apparent appeal of 2D systems. However, they may be circumvented and new opportunities may arise by adopting different strategies. These range from the use of recently discovered 2D magnetic materials ($CrSe_2$, VSe_2, etc.) to the exploitation of the spin–charge interconversion (SCI) that takes place in materials with large spin–orbit coupling (SOC), among which we find TMD semimetals and topological insulators (TIs). The SCI enables electrical generation of spin currents or spin densities, which in turn can be used to generate a torque on an adjacent FM, thus allowing for all-electrical manipulation of the magnetization direction in the FM.

SOC is the responsible interaction for the locking between the spin and the orbital angular momenta and results in a large number of physical phenomena, such as magnetic anisotropy and damping,[30,31] spin relaxation,[32] and the spin Hall effect (SHE).[33,34] The latter is of particular importance for spintronic technologies because it offers a route for the electrical generation of spin currents, one of the most crucial limiting factors in current devices. This is why in recent years much attention is drawn toward materials presenting large SOC and inversion symmetry breaking, both needed for most of the spin–orbit phenomena of interest. In addition, a particular type of SOC that enables the direct coupling between the spin of the electron and its linear momentum can be used for the electrical generation of non-equilibrium spin density, offering a different path for the electrical manipulation of magnets through the spin. Such an effect is referred to as the inverse spin galvanic effect (iSGE) or the Rashba–Edelstein effect.

Recently, researchers proposed to use the iSGE[35,36] and SHE[37,38] to generate current-driven spin–orbit torque (SOT), enabling the electrical manipulation of ultrathin magnets.[39–41] The recent observation of current-driven magnetization switching in inversion symmetry broken transition metal systems (Pt/Co,[42] Ta/NiFe,[43] etc.) initiated a massive amount of effort in this direction. Ultrafast switching was demonstrated,[44,45] and SOT is currently considered a promising method for the next generation of magnetic random-access memories, as explicitly stated in the international roadmap for devices and systems and currently being pursued by major industries.[45]

Among the vast catalog of novel 2D materials, TMDs stand out as a versatile platform for the advancement of disruptive flat microelectronics and spintronics.[5,6,11,46–48] Indeed, in contrast to graphene, TMDs have a large SOC[49–51] that was successfully exploited for gate-controlled spin manipulation in graphene/TMD interfaces.[25,26,52] In addition, some TMDs, such as WS_2 and MoS_2, possess a large bandgap that promotes optoelectronic operation[53,54] and the realization of light-driven spin–valley coupling.[55–60] Beyond the most commonly found semiconducting phase, the TMD family also exhibits a wide variety of electronic behaviors ranging from a Weyl semi-metallic state[61–63] to superconductivity[64,65] as well as magnetism.[66] These features are particularly appealing for the realization of vdW heterostructures[50,51] that could combine all of them.[25,26]

Another important class of vdW materials concern bismuth-antimony chalcogenides that display topological properties. TIs have an insulating bulk and spin–orbit coupled surface states.[67,68] The large spin-momentum locking of their surface states makes them ideal candidates for SCI. Recent progress includes the realization of current-driven SOT in systems using Bi-chalcogenide TIs (Bi_2Se_3/NiFe)[69,70] and the realization of current-driven switching at room temperature[71–73] with record low currents required. Note that SOT also was realized using TMD monolayers[74,75] but with a much weaker efficiency as compared to TIs.

In this Perspective, we present the current state of the art and perspectives on the control of SCI in vdW materials toward the realization of ultra-compact spintronic devices. The complexity of the studied phenomena and the continued surge of new materials make synergy between experiment and theory particularly useful in developing improved large-scale growth methods of such vdW materials to facilitate their implementation in upcoming technologies.

II. GROWTH AND MANIPULATION OF 2D MATERIALS AND VDW HETEROSTRUCTURES

A. Chemical vapor deposition (CVD)

Currently, most 2D materials for fundamental research are produced by mechanical exfoliation, which ensures high crystal quality but with limited yield and size.[76] Since the report on the synthesis of graphene using chemical vapor deposition (CVD),[77] in which volatile precursors react or decompose, this method developed into a popular and reliable technique for the synthesis of different 2D materials, such as h-BN, MoS_2, WSe_2, CrI_3, CrTe, MoSSe, and 2D vdW heterostructures[50,78] (Fig. 1).

For wafer-scale synthesis of 2D materials, a number of approaches were developed, including precise control of the growth process,[79–81] substrate engineering,[82–84] chemical doping,[85–87] transfer,[88–90] surface morphology,[91–93] and twisted bilayers.[94–96] Interestingly, adlayer-free large-area single-crystal graphene was realized on single-crystal Cu foil,[97] which was obtained from commercial Cu foil by the contact-free annealing method.[98] The CVD growth of h-BN, a popular 2D insulator resembling the hexagonal crystal structure of graphene, and 2D heterostructures of h-BN with graphene and TMDs attracted great interest.[99–101] For example, large-area high-quality h-BN was synthesized on single-crystal Cu.[102]

Many 2D materials with excellent semiconductor characteristics and high current on/off ratios, such as MoS_2, $MoSe_2$, WS_2, and WSe_2, were fabricated using CVD.[78,103,104] In particular, stable and controllable growth of large-scale MoS_2 films was achieved by a number of research groups.[105,106] A growth and transfer method of large-area high-quality single-crystal MoS_2 was also reported.[107] Using S and MoO_3 as the growth source and Ar and Ar/O_2 as

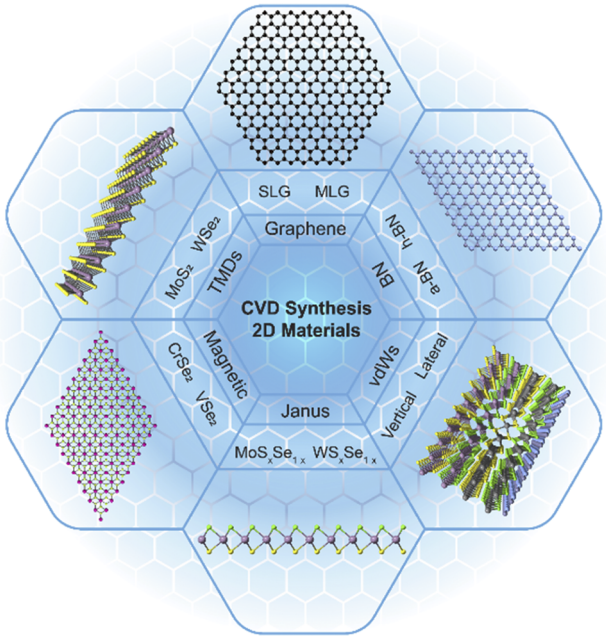

FIG. 1. 2D materials synthesized by the CVD method: graphene, BN, TMDs, magnetic 2D materials, 2D Janus materials, and 2D van der Waals heterostructures.

the carrier gas, the growth was successfully achieved at 930 °C on the sapphire substrate. In addition to MoS_2, there were attempts to grow $MoSe_2$ by CVD.[108,109] A promoter-assisted liquid-phase CVD method was reported to synthesize high-quality large-area monolayer $MoSe_2$.[110] A method to grow wafer-scale monolayer WS_2 used H_2S gas instead of sulfur powder, as the sulfur source reacts after decomposition with WO_3 powder, eventually leading to a 4-in. wafer-scale single-layer WS_2 film.[111] Going beyond individual TMDs, synthesis and precise control of 2D vdW heterostructure arrays was also achieved.[112]

For applications in the field of spintronics, potential magnetic 2D materials include FeX_2, CoX_2, NiX_2, VX_2, CrX_2, and MnX_2 (X = I, Br, and Cl).[113] For the synthesis of large-scale 2D transition metal tellurides by CVD, the use of a mixture of Cr, $CrCl_3$, and Te was reported to lead to a CrTe film.[114]

B. Molecular beam epitaxy (MBE)

An alternative method to grow large-scale 2D materials is molecular beam epitaxy (MBE), a physical deposition technique based on co-evaporation of individual elements under ultra-high vacuum on a crystal surface held at a controlled temperature (Fig. 2). Directional molecular beams are produced by thermal evaporation in effusion cells or by electron-beam evaporation. MBE yields materials with high crystalline quality and centimeter-scale areas. The ultra-high vacuum environment ensures minimal contamination and offers the possibility to use surface analysis techniques to characterize *in situ* the properties of the films. The film composition, doping, and thickness can be accurately controlled, thanks to the low fluxes (typically 1–10 Å/min). Heterostructures consisting of a stack of vdW materials can be formed with abrupt interfaces and an arbitrary number of layers. The growth of layered materials by MBE is based on the method of vdW epitaxy, consisting in film growth either on a passivated surface with a very low density of dangling bonds [e.g., F-terminated $BaF_2(111)$] or on a layered vdW substrate (e.g., SiC/graphene or mica).[116] The weak interaction between the epilayer and the substrate largely releases the constraint of lattice matching and leads to the formation of fully relaxed layers. The advantage of vdW epitaxy is the potential to arbitrarily combine vdW materials with atomically sharp interfaces, free from contaminants.

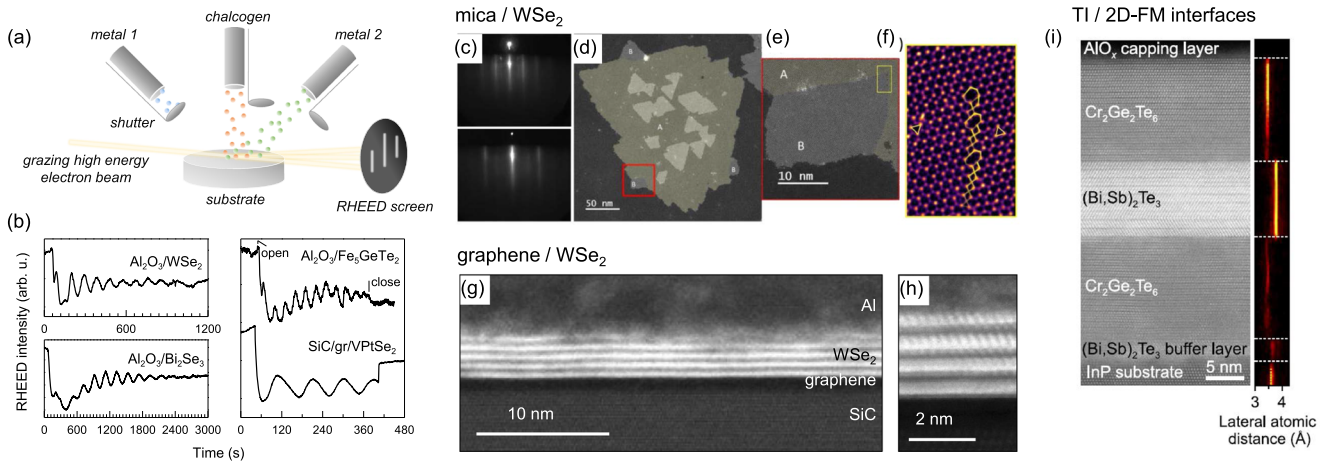

FIG. 2. (a) Schematics of the MBE deposition technique. (b) Reflection high-energy electron diffraction (RHEED) intensity oscillations recorded during the epitaxy of various vdW materials, showing layer-by-layer growth. (c)–(f) Characterization of a WSe_2 monolayer grown by MBE on mica. (c) RHEED patterns in two azimuths showing the single crystallinity of the film. (d)–(f) Plane-view transmission electron microscopy near the boundary between in-plane rotated twin domains (marked A and B). (g) and (h) Cross-sectional high-angle annular dark-field scanning transmission electron microscopy (HAADF-STEM) image of a multilayer WSe_2 film grown on SiC/graphene. (i) Cross-sectional HAADF-STEM image of a $Cr_2Ge_2Te_6/(Bi,Sb)_2Te_3/Cr_2Ge_2Te_6$ epitaxial heterostructure [reproduced with permission from Mogi *et al.*, Phys. Rev. Lett. **123**, 016804 (2019). Copyright 2019, American Physical Society].[115]

The epitaxial growth of layered TIs by MBE was reported on various substrates [e.g., graphene, Si(111), Al_2O_3(0001), GaAs(111), Ge(111), BaF_2(111), InP(111), and $SrTiO_3$(111)].[117–123] Crystals of high quality are commonly produced, but suppressing defects such as chalcogen vacancies or twin boundaries requires fine optimization of the growth parameters.[118,120,123] It is possible by MBE to adjust in $(Bi_{2-x}Sb_x)(Te_{3-y}Se_y)$ alloys the Dirac point energy through the Te/Se ratio[124] and the chemical potential through the Bi/Sb relative content,[119,120] yielding bulk-insulating materials with designed topological Fermion dynamics. Magnetic doping of $(Bi_{2-x}Sb_x)Te_3$ with Cr and V[125–128] as well as epitaxy of the antiferromagnets $MnBi_2Se_4$[129,130] and $MnBi_2Te_4$[131,132] were reported, enabling the experimental realization of the quantum anomalous Hall effect.[133] For the large-area growth of TIs, other physical deposition techniques were employed recently, such as sputtering and pulsed laser deposition.[73,134]

Efforts in the MBE of TMDs are more recent. Epitaxy was reported for a variety of TMDs and TMD heterostructures, including $MoSe_2$, WSe_2, $HfSe_2$, $PtSe_2$, VSe_2, $ZrTe_2$, $MoTe_2$, and WTe_2.[66,135–149] Inert vdW surfaces, such as graphene, mica, or hBN, make it possible to stabilize very flat monolayers of high structural quality, as shown for mica/WSe_2.[149] However, the weak interfacial interaction often results in an in-plane misorientation of crystal grains, which probably remains the main difficulty in the MBE of TMD monolayers. The misorientation is due to atomic position coincidences between the TMD monolayer and the substrate, favoring the formation of grains with an orientation away from the exact epitaxial relationship. These configurations being metastable, high-temperature growth and/or post-deposition annealing might improve the in-plane crystal quality. Another strategy consists in orienting the grains by nucleation at step edges using vicinal surfaces. In addition, quasi-vdW epitaxy on non-vdW surfaces may promote a better crystal alignment at the expense of a stronger substrate interaction[146] and a possible loss of the intrinsic TMD properties. Recently, substrate-induced strain was used to stabilize the metastable semimetallic 1T′ phase in WSe_2[150] and WTe_2.[151]

Reports on the MBE of 2D-FMs include diluted magnetic TMDs, such as V-doped WSe_2[152,153] and Mn-doped $MoSe_2$,[154,155] intercalated vdW compounds, such as V_5Se_8[156] and Cr_2Te_3,[157] and intrinsic FMs, such as $Cr_2Ge_2Te_6$,[158] Fe_3GeTe_2,[159–161] $CrBr_3$,[162] $CrCl_3$,[163] and CrI_3.[164] Intrinsic ferromagnetism was also claimed for MBE-grown monolayer $MnSe_x$[165] and VSe_2,[66] although in the latter case, a charge density wave tends to suppress ferromagnetism.[166,167] TI/2D-FM multilayers with abrupt epitaxial interfaces were achieved by MBE only recently.[158,161]

III. FABRICATION OF DEVICES

SCI can be probed and exploited in different types of spintronic devices. The two most prominent examples are the non-local Hall cross spin devices and the SOT devices. The non-local Hall cross devices [sketched in Fig. 3(a)] combine different materials with specific purposes. In the case of vdW heterostructures, they consist of a spin channel made of a low-SOC material (typically

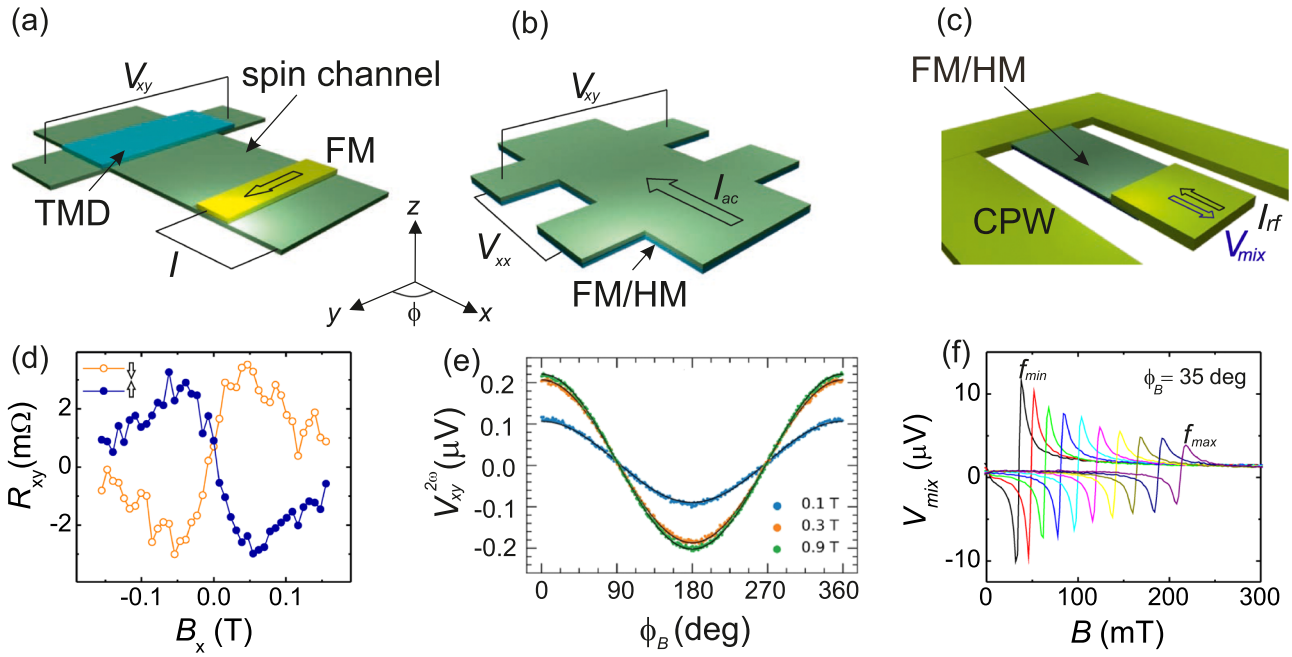

FIG. 3. Schematic illustration of the (a) non-local lateral device, (b) second-harmonic Hall device, and (c) SOT-FMR device. (d) Representative room-temperature non-local resistance ($R_{xy} = V_{xy}/I$) vs magnetic field (B_x) measurements in the iSHE configuration in a graphene-WS_2 device. Open and closed symbols correspond to the magnetization of the FM aligned in the −y and +y directions, respectively. (e) Representative second-harmonic Hall voltage for a TMD/NiFe bilayer as a function of the angle between the in-plane magnetic field and the direction of the current for different magnitudes of the magnetic field. (f) Typical SOT-FMR resonances in a TMD/NiFe bilayer for different frequencies with the in-plane magnetic field applied at 35° relative to the direction of the current. The characteristic resonance frequencies f_{min} and f_{max} are in the 1–20 GHz range. (d) Adapted with permission from Benítez *et al.*, Nat. Mater. **19**, 170–175 (2020). Copyright 2020, Springer Nature Limited. (e) Adapted with permission from Gupta *et al.*, Nano Lett. **20**, 7482–7488 (2020). Copyright 2020, American Chemical Society.

graphene) where the spins can propagate over long distances (tens of μm). Spins are injected and detected either through a FM or by taking advantage of SCI in materials with large SOC. Due to the atomically thin nature of graphene, its very weak SOC can be enhanced by proximity effects when stacking the material with other vdW materials, including TMDs, semimetals, and TIs, which are characterized by large SOC.

As the *in situ* growth of vdW heterostructures is still at an early stage, most of the studied systems to date are obtained by stacking mechanically exfoliated crystals. Owing to the nature of the studied effects and stability issues of some of the utilized materials at ambient conditions, the heterostructures are fabricated under controlled atmosphere with a low concentration of H_2O and O_2 (around 0.1 ppm), thus providing at the same time ultra clean interfaces. The stacks are obtained by transferring the 2D materials using a dry transfer method, in which viscoelastic stamps are used to pick-up and release flakes in a controlled manner. Precise alignment between the flakes is achieved by using a micro-positioner stage and an optical microscope. To avoid gas bubbles and blisters and to ensure better attachment between the layers, the finished stacks are usually annealed in an Ar/H_2 atmosphere or high vacuum.

The stacking process is followed by electron-beam lithography and reactive etching steps to define electrical contacts and to pattern the heterostructure with specific shapes and dimensions. Devices for SCI experiments consist of graphene etched in a Hall bar geometry. The graphene channel, typically 1 μm wide and tens of μm long, includes a graphene Hall arm capped with a large-SOC material (see Sec. IV for further details). The device includes a combination of metal and FM contacts. Metal contacts, typically Ti/Au or Ti/Pd, are attached to the graphene Hall cross and can be used either for applying an electric current or for measuring the voltage along the Hall bar. FMs (typically Co) are used to both inject and detect the spin current. Efficient spin injection and detection require the insertion of thin insulating barriers between the FM contacts and graphene to alleviate the conductance mismatch.[168,169]

SOT devices are made of bilayer heterostructures of FMs and large-SOC materials, the device geometry depending on the measurement technique [Figs. 3(b) and 3(c)]. In the case of SOT ferromagnetic resonance (FMR) experiments [Fig. 3(c)], large-SOC/FM bilayers are embedded into high-frequency coplanar waveguides, whereas for harmonic Hall voltage measurements, the bilayer is patterned in a Hall bar geometry [Fig. 3(b)]. Most of the vdW-based SOT devices studied to date feature heterostructures combining vdW materials with well-known bulk systems. Various studies considered mechanically exfoliated TMD flakes (under vacuum or flowing N_2, or in a glovebox with inert Ar atmosphere) with a thin film of a FM (typically NiFe due to its low magnetic damping) deposited on top. Further studies spanned from exfoliated crystals to materials grown by CVD (TMDs such as MoS_2 or WSe_2[74,170]) or MBE [TIs such as Bi_2Se[69,70] and $(Bi_{1-x}Sb_x)_2Te_3$[171,172]]. The FM is deposited using grazing angle sputtering in various reports, to avoid damaging the underlying TMD, and capped to prevent oxidation. Similarly, vdW FMs, such as Fe_3GeTe_2 and $Cr_2Ge_2Te_6$, obtained from exfoliation methods can be combined with heavy-metal layers of Pt and Ta. Due to the high sensitivity of these 2D FMs to ambient conditions, they are typically rapidly transferred to a deposition chamber and the heavy metal layer is sputtered on top[173,174] (in some cases, preceded by a short etching with Ar plasma to clean the interface[175,176]).

SOT devices (with sizes of up to 20 × 100 μm^2) are commonly patterned either by electron beam or by optical lithography techniques, followed by ion milling and the deposition of metal contacts. However, when investigating magnetization switching mechanisms, it is important to take into account the dimensions of the device; for large devices, switching occurs by domain nucleation and motion, which results in low switching currents. To date, fewer studies were realized for all-vdW SOT devices. These include *in situ* MBE-grown $(Bi_{0.5}Sb_{0.5})_2Te_3/(Cr_{0.08}Bi_{0.54}Sb_{0.38})_2Te_3$ bilayers with a capping, which were patterned by photolithography and dry etching.[177] More recently, switching of Fe_3GeTe_2 on WTe_2 was reported.[178] The samples were prepared similarly to the above-mentioned lateral structures by dry transfer of mechanically exfoliated flakes inside an inert Ar atmosphere glove box, further protected by electron-beam evaporated Al capping. Progress in the *in situ* growth of vdW heterostructures may greatly simplify the fabrication steps required to preserve the interfaces from degradation due to air exposure.[161]

IV. SCI: EXPERIMENTS

A. Non-local Hall cross devices

Pioneering SCI experiments were conducted in metallic systems using non-local detection techniques. These devices use a FM contact for injecting spins into a non-magnet, typically Cu and Al, acting as the spin transport channel. Spins diffuse and are absorbed by a heavy-metal, e.g., Pt and Ta, in which a transversal voltage, generated by the iSHE, is measured in a Hall cross geometry.[33] Later, the same geometry is used by replacing the spin transport channel by graphene (see hybrid systems in Table I), providing a highly efficient spin injection that results in enhanced measured SCI efficiencies.

Over the last few years, SCI in lateral spin devices regained attention. The rich variety of vdW materials and possible combinations opened up the possibility to realize SCI in all-vdW systems. When combining graphene, which possesses excellent spin transport properties, with a non-conducting vdW material with large SOC, typically a semiconducting TMD, SCI occurs in graphene due to proximity effects. In the graphene/TMD region, the SOC of graphene is enhanced and the electronic band structure is modified significantly, with the most prominent features being the opening of an energy gap in the meV range at the K and K′ points, lifting of spin degeneracy, and imprinting of an out-of-plane spin texture (with the spin orientation depending on the valley and a winding in-plane component far from the charge neutrality point).[179]

The device geometry [as sketched in Fig. 3(a)] is slightly different and consists of a graphene Hall cross with one of its arms shrouded with a TMD. The pristine graphene region (not covered by the TMD) is used to transport spin information from the spin injector to the Hall arm and vice versa. A spin current is injected into graphene by means of a planar FM contact with magnetization along its long axis.[10] When diffusing toward the Hall arm region, the spins experience precession under an external magnetic field. The relative direction between the magnetic field and the injected spins is key to distinguish between the different spin-to-charge conversion mechanisms (SGE or iSHE). In the case of the SGE, an out-of-plane

TABLE I. SCI efficiencies in non-local devices based on metallic, hybrid, and all-vdW systems. The parameters are defined as follows: $\gamma^{SH} \equiv j_c^y/j_s^z$; $\alpha^{SGE} \equiv j_c^y/j_s^x$ (see *x*, *y*, and *z* directions in Fig. 3); j_c^y is the charge current flowing along the *y* direction, i.e., along the Hall cross; j_s^z is the spin current along the *z* direction (arising from the iSHE); j_s^x is the spin current along the *x* direction (arising from the SGE); $\lambda_s^{\perp}$ and $\lambda_s^{\parallel}$ are the spin relaxation lengths of spins precessing in-plane and out-of-plane, respectively; and $\alpha^{*\,SGE} \equiv 2RE v_F \rho \tau^{\parallel}$, with *RE* being the strength of the SGE, ρ being the resistivity of the graphene beneath the TMD, v_F being the Fermi velocity, and $\tau^{\parallel}$ being the spin lifetime of the in-plane spins.

	Comments	SCI mechanism	SCI (%)	SCI efficiency (nm)	References
			Metallic		
Cu/Ta	ρ (Ta) = 333 $\mu\Omega$ cm (10 K) λ_s (Ta) = 2.7 nm (10 K)	iSHE	γ^{SH} (Ta) = −0.37 ± 0.20 (10 K)	$\gamma^{SH}\cdot\lambda_s$(Ta) = 0.01 (10 K)	180
Cu/Pt	ρ (Pt) = 17.9 $\mu\Omega$ cm (RT) λ_s (Pt) = 7 nm (RT)	iSHE	γ^{SH} (Pt) = 0.9 (RT)	$\gamma^{SH}\cdot\lambda_s$(Pt) = 0.06 (RT)	181
Cu/Pt	ρ (Pt) = 44.1 $\mu\Omega$ cm (10 K) λ_s (Pt) = 0.75 nm (10 K)	iSHE	γ^{SH} (Pt) = 8.5 ± 1.3 (10 K)	$\gamma^{SH}\cdot\lambda_s$(Pt) = 0.06 (10 K)	182
			Hybrid		
Bi_2O_3/graphene	Bilayer graphene	iSHE (in proximitized graphene)	γ^{SH} = 0.10 ± 0.05 (RT) γ^{SH} = 0.6 ± 0.1 (10K)	λ_s not measured in the SCI region	183
Pt/graphene	Single-layer graphene ρ (Pt) = 46 $\mu\Omega$ cm (RT) λ_s (Pt) = 5 nm (RT; taken from the literature)	iSHE (in Pt)	γ^{SH} (Pt) = 15 ± 1 (RT)	$\gamma^{SH}\,\lambda_s$(Pt) = 0.75 (RT)	184
Pt/graphene	Few-layer graphene ρ (Pt) = 134 $\mu\Omega$ cm (RT) λ_s (Pt) = (2.1 ± 0.4) nm (RT) (taken from the literature)	iSHE (in Pt)	γ^{SH} (Pt) = 23.4 ± 2.5 (RT)	$\gamma^{SH}\,\lambda_s$(Pt) = 0.50 ± 0.02 (RT)	185
			All-vdW		
MoS_2/graphene	Few-layer graphene Spin absorption by MoS_2	iSHE (in proximitized graphene and MoS_2)	γ^{SH} = −0.33 ± 0.04 (RT) γ^{SH} = −4.5 ± 0.9 (10 K)	λ_s not measured in the SCI region	186
WS_2/graphene	Single-layer graphene	SHE–iSHE (in proximitized graphene)	γ^{SH} = 0.3 (RT)	$\gamma^{SH}\cdot\lambda_s^{\perp}$(gr/$WS_2$) = 3.75 (RT)	187
	(Non-conducting) multilayer WS_2 $\lambda_s^{\perp}$(gr/WS_2) = 1.25 μm $\lambda_s^{\parallel}$(gr/WS_2) = 420 nm	SGE–iSGE (in proximitized graphene)	α^{ISGE} = 0.1 (RT)	$\alpha^{ISGE}\cdot\lambda_s^{\parallel}$(gr/$WS_2$) = 0.42 (RT)	

TABLE I. (*Continued.*)

	Comments	SCI mechanism	SCI (%)	SCI efficiency (nm)	References
WS_2/graphene	Single-layer graphene (Non-conducting) single-layer WS_2 $\lambda_s^{\perp}$ (gr/WS_2) = 1.58 μm $\lambda_s^{\parallel}$ (gr/WS_2) = 313 nm	SHE–iSHE (in proximitized graphene) SGE–iSGE (in proximitized graphene)	γ^{SH} = 0.13 (4 K), vanishes at $T > 20$K α^{*SGE} = 2.8 (4 K) α^{*SGE} = 0.56 (RT)	Different definition of α^{*SGE} (see the table caption)	188
WSe_2/graphene	Few-layer graphene Spin absorption by WSe_2	iSHE (in proximitized graphene)	γ^{SH} = 1.7 ± 0.2 (RT) γ^{SH} = 2.8 ± 0.3 (10 K)	λ_s not measured in the SCI region	189
2H–TaS_2/graphene	Few-layer graphene Multilayer TaS_2 (metallic)	SGE–iSGE (in proximitized graphene and TaS_2)	α^{SGE} = −1.4–4.3 (RT) (Gate-tunable)	λ_s not measured in the SCI region	190
$(BiSb)_2Te_3$/graphene	Single-layer graphene Multilayer BST	SGE (in proximitized graphene)	α^{SGE} = 0.17; 2.5; 1; 4.8 (RT)	λ_s not measured in the SCI region	191
$MoTe_2$/graphene	Few-layer graphene Multilayer $MoTe_2$	Unconventional SCI (in $MoTe_2$)	$\alpha^{SCI} \geq 0.21$ (RT) (conventional) $\alpha^{SCI} \geq 0.10$ (RT) (unconventional)	λ_s not measured in the SCI region	192
WTe_2/graphene	Single-layer graphene Multilayer WTe_2 λ_s (WTe_2) = 8 nm	Unconventional SCI (in WTe_2)	α^{SCI} = 9 (RT)	$\alpha^{SCI} \cdot \lambda_s$ (WTe_2) = 0.72 (RT)	193

magnetic field causes an in-plane spin precession leading to a voltage along the Hall arm driven exclusively by the SGE. In the case of the iSHE, a magnetic field is applied to graphene along the spin diffusion channel. The spins diffusing toward the Hall cross precess out-of-plane, generating a voltage driven exclusively by the iSHE [Fig. 3(d)].

For the reciprocal effect, i.e., charge-to-spin conversion, a charge current flowing along the Hall arm generates a transversal spin current and a non-equilibrium in-plane spin density due to the SHE and the iSGE, respectively. In the case of the SHE, the spins point out-of-plane, whereas in the case of the iSGE, a non-equilibrium spin density with the spins pointing in-plane and perpendicular to the charge current is generated at the graphene/TMD interface. These two spin components (perpendicular to each other) can be probed by a FM acting as a spin detector, with the magnetization perpendicular to both spin components, and are disentangled by varying the direction of the external magnetic field.

SCI experiments in lateral spin devices were initially reported for multilayer graphene combined with MoS_2.[186] Shortly after, spin–charge interconversions driven by both the SHE and SGE were probed in the graphene-WS_2 heterostructure at room temperature.[187,188] Remarkably, both SCI mechanisms exhibit a gate-tunable magnitude that can be controlled by electrostatic gating. This knob is, in fact, essential to determine whether the SCI occurs exclusively in graphene. The electrostatic gating not only varies the carrier density in the graphene layer but also shifts the Fermi energy in the TMD. The latter may alter the insulating character, resulting in spin absorption and related SCI within the TMD if the Fermi level shifts toward the conduction (or valence) band. More recently, SCI driven only by the SHE was reported for the graphene-WSe_2 heterostructure.[189]

Beyond semiconducting TMDs, SCI experiments combining graphene with other large-SOC materials were also reported for Bi_2O_3,[183] metallic layered 2H–$TaSe_2$,[190] the layered p-type TI $(Bi_{0.15}Sb_{0.85})_2Te_3$,[191] and the semimetals 1T′-$MoTe_2$[192] and WTe_2.[193] Overall, the SCI efficiency in all-vdW heterostructures, defined as $\gamma^{SH}\cdot\lambda_s$ with λ_s being the spin relaxation length in the region where the SCI takes place, compares favorably with fully metallic or hybrid systems based on heavy metals, such as Pt and Ta. Table I summarizes experimental measurements of the SCI efficiency for metallic systems, hybrid systems, and all-vdW heterostructures, specifying which SCI mechanism takes place and where. We note that some studies consider an effective λ_s^{eff} of the whole channel (not only the SCI region, i.e., include a large contribution of regular graphene). These values are not included in Table I, as they could overestimate the SCI efficiency.

B. SOT devices

Aside from the non-local Hall cross, two other methods are commonly employed to study the SCI in TMD/FM and TI/FM bilayers [Figs. 3(b) and 3(c)]. The second-harmonic Hall (2ω-Hall)[194] and SOT ferromagnetic resonance (SOT-FMR)[37] techniques both measure the current-driven SOT in the FM, from which the charge-to-spin conversion efficiency is inferred. Additionally, the spin pumping effect, based on the reciprocal effect of spin transfer, can be used to measure the SCI efficiency.[195] In 2ω-Hall and SOT-FMR experiments, the current-driven SOT induces precession of the magnetization, which results in time-dependent changes in the longitudinal and transverse resistances. Frequency mixing between the resistance and current oscillations leads to measurable direct current and second-harmonic voltages [Figs. 3(e) and 3(f)]. The magnitude, direction, and nature (conservative/dissipative) of the SOT are deduced from the field and angle dependences of these voltages. In spin pumping experiments, magnetization precession is driven by an external microwave magnetic field. Spins aligned with the average magnetization are pumped into the adjacent large-SOC material, where spin-to-charge conversion gives rise to a measurable direct charge current.

Because of the spin-polarized surface states of TIs, the TI/3D-FM bilayers are among the most widely used SOT systems that include vdW materials. Seminal works showed very large SCI efficiencies for Bi_2Se_3/NiFe[69] and Bi_2Se_3/CoFeB.[70] A strong Fermi level dependence of the SOT was found in $Bi_xSb_{2-x}Te_3$/NiFe,[171] and electrostatic gating of the SOT was demonstrated in magnetic Cr-doped $Bi_xSb_{2-x}Te_3$.[196] A large in-plane damping-like SOT is generally observed, enabling efficient current-driven magnetization switching.[196,197] Noteworthy, there is less evidence of large field-like SOT, expected to be a clear signature of the iSGE. The reported damping-like SOT efficiency is typically 0.1–1, which is significantly larger than in heavy metals.[41] The corresponding Edelstein inverse length q is in the range 0.1–1 nm^{-1}.[171,172] On the other hand, the Edelstein length λ measured with spin pumping is typically 0.01–0.1 nm,[198] which is rather low in comparison to other 2D systems (0.2–0.4 nm for the Bi/Ag Rashba interface[199] and 2.1 nm for the surface of the α-Sn TI[200]).

SOT measurements were reported for various TMD/3D-FM bilayers.[201] Semiconducting (MoS_2, WS_2, and WSe_2), semimetallic (WTe_2, β-$MoTe_2$, $TaTe_2$, and $PtTe_2$), and metallic ($NbSe_2$ and TaS_2) TMDs were interfaced with NiFe, Co, or CoFeB. Salient results are the gate-modulation of the SOT with WS_2[202] and the generation of unconventional SOT with low-symmetry TMDs.[203,204] ST-FMR measurements of 1T′-WTe_2/NiFe devices revealed an unusual out-of-plane damping-like SOT whose magnitude depends on the direction of the current with respect to the crystallographic axes, reflecting the reduced symmetry of the bilayer.[203,204] 2ω-Hall measurements in similar bilayers showed an anisotropic field-like SOT, which was attributed to the contribution of topological Fermi arcs.[205] The reported SOTs are generally weaker with TMDs than with TIs. Nonetheless, efficient and field-free current-driven magnetization switching was recently achieved in WTe_2/NiFe.[206] Further work is required to clarify the SCI mechanisms at play with TMDs, as contrasting results were reported about the damping-like/field-like SOT ratios and the bulk or interfacial origin of the SOT. Spin pumping studies of TMD/FM systems are still scarce. Spin pumping measurements of MoS_2/YIG yielded an Edelstein length λ of 0.4 nm.[207]

More recently, the SOT was studied in large-SOC/2D-FM heterostructures, with significant efficiencies and magnetization switching reported in Fe_3GeTe_2/Pt.[173,175] Single 2D-FM layers are also interesting candidates for the generation of unconventional SOT. For example, the low symmetry of monolayer Fe_3GeTe_2 allows for a SOT akin to a current-driven magnetic anisotropy.[208,209] Experimental hints of such a SOT were also reported for multilayer Fe_3GeTe_2.[210]

In contrast to lateral spin devices in which the spin injection, transport, and detection are spatially well separated, these processes occur in vertical bilayers within a couple of nanometers near the interface. As recently shown for TI/FM bilayers,[172] the SOT is thus extremely sensitive to the structural, chemical, and electronic properties of the interface, where band bending, orbital hybridization, spin memory loss, material intermixing, and magnetic dead layers were reported.[211–215] These phenomena are generally detrimental to the SOT, complicate the analysis of the SCI, and are probably responsible for the large experimental spread in the SCI efficiencies. It is expected that all-vdW heterostructures combining 2D-FMs with TIs or TMDs will display enhanced SOT and will constitute model systems, thanks to their sharp and weakly interacting interfaces. Indeed, a recent study found a SOT efficiency of 4.6 in WTe_2/Fe_3GeTe_2.[178]

Apart from the novel spin phenomena due to proximity effects between different vdW materials, there is promise to solve a challenge that exists in today's magneto-resistive random access memory technology. Here, perpendicular magnetization switching is more attractive because it is faster and more scalable. Efficiently switching a perpendicular magnetization using SOT requires the spins to have a large out-of-plane component (out-of-plane anti-damping SOT), which is very difficult to realize by common materials. Recent evidence shows that vdW materials with low-crystalline symmetry, in principle, can be used to control the direction of the current-induced SOT.[204,216] A summary of experimental parameters describing the SCI in vdW-based SOT devices is given in Table II.

V. SCI: THEORETICAL CONTRIBUTIONS

Successful integration of vdW heterostructures in the technological workflow relies on achieving efficient electrical control. For low-power applications, where a small current flow is essential, linear response theory provides a general framework to determine any observable electrical response. The central figure of merit of the SCI is the spin Hall angle γ_{sH}, which determines the amount of pure spin current generated for an incoming charge current.[33] For quantifying the SOT efficiency, it is usual to evaluate the torque efficiency χ_τ, which measures the amount of torque felt by a magnet per unit of current density and can be rewritten as an effective spin Hall angle.[41] The crystal symmetries prescribe the spin orientation via the SOC. In combination with group theory, the theory of invariants enables a relatively straightforward method to determine the allowed directions.[217,218] First, one identifies the minimum set of point symmetries capable of expanding the whole point group (generating elements) and then imposes invariance of the linear response tensor with respect to those symmetries. By doing so, one finds a set of constraints limiting the number of finite elements and fixes the allowed directions for a given current.

The combination of disorder, exchange interaction, and SOC defines the efficiencies. Therefore, it is essential to properly describe the band structure, spin texture, and exchange splitting of the considered vdW system and evaluate the role of disorder in the diffusive regime, which is the most common experimental situation.[219–221] Recent reports suggest that the use of symmetry-based models derived from *ab initio* methods provides the most cost-effective way to describe simple systems, such as graphene[220] and WTe_2.[222] However, although computationally inefficient, Wannier Hamiltonians are the preferred choice for more complex vdW heterostructures.[223,224] On the other hand, linear scaling quantum transport methodologies are the only computational approaches capable of addressing the diffusive regime, since the systems involved demand for models containing many millions of atoms.[225] Most of these methods are numerical implementations of the Kubo formula, either in the time or energy domain, allowing us to determine a system's properties for different transport regimes.

For honeycomb-based vdW heterostructures, spin–valley coupling and broken inversion symmetry make the two valleys inequivalent in terms of the spin and Berry curvature, providing a unique platform for efficient SCI.[186,187,222,226,227] In Fig. 4, we present a sketch of how lowering the symmetries enables modifications in the band structure that enable different spin-related effects. In a highly symmetric system, such as graphene, combination of the inversion and time-reversal symmetries does not allow for spin-momentum locking and, therefore, prevents the Rashba–Edelstein effect and its associated SOTs. In TMDs, the presence of chalcogen and metal atoms lifts the inversion symmetry and enables band-splitting due to the SOC. However, since there is a horizontal mirror plane, the system cannot host a vertical electrical field, which prevents the typical in-plane spin-momentum locking. Yet, the broken inversion symmetry enables a novel torque not related to the Rashba effect that acts as an electrically controlled magnetic anisotropy, which is a promising gateway to magnet-free switching of perpendicular magnetizations.[228] In honeycomb-based heterostructures, the presence of dissimilar layers finally removes the horizontal mirror plane and reduces the symmetry to a C_{3v} point group, which supports the conventional field-like and damping-like torques, as well as an electrically controlled magnetic anisotropy,[228] as demonstrated experimentally in $L1_1$ CoPt/CuPt bilayers.[229] However, this switching depends on the threefold rotation, and systems such as graphene and TMDs, where the Fermi level lies on an isotropic surface, are not expected to display the effect. Recently, tremendous efforts focused on synthesizing a new class of materials, the magnetic Janus TMDs, built by replacing the chalcogen atoms on one side of a TMD with different ones. Janus materials show simultaneously spin–valley coupling and a large Rashba effect due to their intrinsic electrical dipole[178] and magnetism due to the presence of magnetic metal atoms.[224] Although Janus materials are still in their infancy, they combine multiple desirable properties for technological applications and deserve scrutiny. For instance, they are ideal for achieving all-in-one SOT, where the magnetization is electrically switchable in a single material via a current.[224]

The valley-driven spin Hall effect is a phenomenon where the electron motion is monitored by a spin-dependent Lorentz force opposite in each valley.[186,187,227] The broken inversion symmetry of heterostructures can also generate a Rashba interaction, which, when combined with spin–valley coupling, leads to valley-dependent SOT[228] and yields optimal SCI via the Rashba–Edelstein effect.[227] The interplay between spin–valley coupling, Rashba interaction, and magnetism is not extensively studied to date. In magnetic systems with a Zeeman splitting, the valley-Zeeman effect[221] leads to valley polarization, as predicted for TMD/2D-magnet heterostructures[230,231] and recently realized in WSe_2/CrI_3.[232] Nevertheless, understanding the combined impact of the valley-Zeeman

TABLE II. SCI in vdW-based SOT devices. The parameters are defined in Ref. 41, where additional non-vdW structures are reviewed. For TMDs, a complementary comparative study can be found in Ref. 201.

	Fabrication	Method	B_{DL}/j	B_{FL}/j	ξ^j_{DL}	ξ^j_{FL}	ξ^E_{DL}	ξ^E_{FL}	q_{REE}	λ_{IREE}	Other torques	References
			mT/(10^{11} A/m^2)		Dimensionless		10^5 $\hbar$/2e (Ωm)$^{-1}$		nm^{-1}	nm		
Non-vdW												
Pt(3)/Co(0.6)/AlO_x(1.6)	Sputtering	2ω-Hall	−6.9	4	0.13	−0.073	3.5	−2				41
Ta(1.5–5)/CoFeB (0.8–1.1)/MgO(2)	Sputtering	2ω-Hall	1.3–4.4	−(2–19)	−(0.03–0.11)	0.04–0.47	−(0.14–0.68)	0.22–0.67				
Bi(8)/Ag(5–20)/Py(15)	Evaporation	Spin pumping								0.2–0.4		199
α-Sn(30 Ml)/Ag(2)/Fe(5)	MBE	Spin pumping								2.1		200
TI												
Bi_2Se_3(8)/Py(8,16)/ AlO_x(2)	MBE	ST-FMR			2.0–3.5[a]	2.5–2.8[b]	1.1–2.0	1.4–1.6				69
Bi_2Se_3(20)/CoFeB(5)/ MgO(1)/SiO_2(3)	MBE	ST-FMR RT ~20 K			 0.05–0.11 ~0.4	 0–0.1 ~0.2						70
Bi_2Se_3(10)/Ag(5)/CoFeB(7)/ MgO(2)/SiO_2(4)	MBE	ST-FMR	5.3	3.2	0.5[c]	0.3[b]						233
Bi_2Se_3(7.4)/ CoTb(4.6)/SiN_x(3)	MBE	Coercivity	6.1		0.16							71
Bi_2Se_3(8)/Py(6)/ MgO(1)/SiO_2(4)	MBE	Coercivity			1.71							72
Bi_2Se_3(5)/CoFeB(7)/ MgO(2)/Al_2O_3(3)	MBE	ST-FMR			1.75				0.82			72
Bi_2Se_3(20)/CoFeB(7)/ MgO(2)/Al_2O_3(3)					0.3[c]				~0.1[c]			
Bi_2Se_3(5–35)/ Py(20)/SiO_2(30)	MBE + Ar milling	Spin pumping			0.0093							234
Bi_2Se_3(5,10)/ CoFeB(5)/MgO(2)	MBE	Spin pumping			0.021–0.43							235
Bi_2Se_3(10)/CoFeB(5)/MgO(2)	MBE	ST-FMR			0.3–1.7							235
Ge/Bi_2Se_3(10)	MBE	Non-local								−0.026[c]		236
Bi_xSe_{1-x}(4)/CoFeB(5)/ MgO(2)/Ta(5)	Sputtering	2ω-Hall ST-FMR	99		18.6 8.7		1.45					73
YIG/Bi_2Se_3(6–60)	MBE	Spin pumping								0.035		237

TABLE II. (*Continued.*)

	Fabrication	Method	B_{DL}/j	B_{FL}/j	ξ^j_{DL}	ξ^j_{FL}	ξ^E_{DL}	ξ^E_{FL}	q_{REE}	λ_{IREE}	Other torques	References
			mT/(10^{11} A/m^2)		Dimensionless		10^5 $\hbar$/2e (Ωm)$^{-1}$		nm^{-1}	nm		
YIG/(Bi,Sb)$_2$Te$_3$(6)	MBE	Spin pumping								0.017		
MgO(2)/Bi$_2$Te$_3$(8)/CoTb(6)/TaO$_x$(1.5)	Sputtering	2ω-Hall	87	~0	3.3							238
(Bi$_{1-x}$Sb$_x$)$_2$Te$_3$(8)/Cu(8)/Py(10)	MBE	ST-FMR										171
x = 0.5, 0.7, 0.9					~0.5[c]				0.45–0.57			
0.8 < x < 0.9					(1–5)[a]				0.1–0.2			
(E_F near Dirac point)												
(Bi$_{0.4}$Sb$_{0.6}$)$_2$Te$_3$(9)/Py(5)/AlO$_x$(2)	MBE	ST-FMR	0.02–0.1 mT/(A/m)[d]	0 < $-B_{FL}$ < B_{Oe}[c]	(0.88)[a]				0.19–0.88			172
(Bi$_{0.4}$Sb$_{0.6}$)$_2$Te$_3$(9)/Ag(7)/Py(5)/AlO$_x$(2)	MBE	ST-FMR	0.01–0.07 mT/(A/m)[d]	$B_{FL} \approx -B_{Oe}$[c]					0.12–0.53			172
(Bi$_{0.4}$Sb$_{0.6}$)$_2$Te$_3$(9)/Al(6)/Py(5)/AlO$_x$(2)	MBE	ST-FMR	0.01–0.06 mT/(A/m)[d]	0 < B_{Oe} < $-B_{FL}$[c]					0.11–0.48			172
Cr$_{0.16}$(Bi$_{0.54}$Sb$_{0.38}$)$_2$Te$_3$(6)/(Bi$_{0.5}$Sb$_{0.5}$)$_2$Te$_3$(3)	MBE	2ω-Hall 1.9 K	48 000 −146 000		140–425[e]							177
Cr$_{0.16}$(Bi$_{0.5}$Sb$_{0.42}$)$_2$Te$_3$(7)/Al$_2$O$_3$(20)	MBE	2ω-Hall 1.9 K	46 900[b]		116[e]							196
(Bi$_{0.22}$Sb$_{0.78}$)$_2$Te$_3$(6)/Py(12)	MBE	Spin pumping								0.075		198
(Bi$_{0.22}$Sb$_{0.78}$)$_2$Te$_3$(6)/NiO(5)/Py(12)	MBE	Spin-Seebeck effect								0.076		198
					TMD							
MoS$_2$(0.8)/CoFeB(3)/TaO$_x$(3)	CVD	2ω-Hall	~0	0.078[b]	~0	−0.14	~0	0.0288				74
WSe$_2$(0.8)/CoFeB(3)/TaO$_x$(3)	CVD	2ω-Hall	~0	0.114[b)]	~0		~0	0.0552				
MoS$_2$(0.8)/Py(5)	CVD	ST-FMR	Large									170
WTe$_2$(1.8–15)/Py(6)/AlO$_x$(2)	Exfoliation	ST-FMR/2ω-Hall			0.03*	~0	0.08	0.09			Out-of-plane DL	204
WTe$_2$(5.6–7)/Py(6)/Ru(4)	Exfoliation	2ω-Hall RT		$B_{FL} \gg B_{Oe}$				~1[f]				205
		<50 K						~2.5[f]				
WTe$_2$(20–31)/Py(6)/Ru(4)	Exfoliation	2ω-Hall RT						~0				205
		<50 K						~4[f]				

TABLE II. (*Continued.*)

	Fabrication	Method	B_{DL}/j	B_{FL}/j	ξ^j_{DL}	ξ^j_{FL}	ξ^E_{DL}	ξ^E_{FL}	q_{REE}	λ_{IREE}	Other torques	References
			mT/(10^{11} A/m^2)		Dimensionless		10^5 ħ/2e (Ωm)$^{-1}$		nm^{-1}	nm		
WTe_2(5.8–122)/Py(6)	Exfoliation	ST-FMR coercivity			0.09–0.79 0.15–0.65	~0	0.02–0.6[f]				Out-of-plane DL	206
YIG/MoS_2(2.4)	Exfoliation	Spin pumping			0.32					0.4		207
$TaTe_2$(4.5–19.7)/Py(6)/AlO_x(2)	Exfoliation	ST-FMR/2ω-Hall	~0	~0	~0	~0	~0	~0				239
$MoTe_2$(0.7–14.2)/Py(6)/AlO_x(2)	Exfoliation	ST-FMR					0.058	0.15			Out-of-plane DL	240
$PtTe_2$(3–20)/Py(2.5–10)	CVD	ST-FMR			0.05–0.15	−0.004	0.2–1.6					241
$NbSe_2$(0.6–6)/Py(6)/AlO_x(2)	Exfoliation	ST-FMR					0.03	0.40			Out-of-plane DL	242
TaS_2(0.88)/Py(7)/AlO_x(3)	Plasma-assisted sulfurization	ST-FMR			0.25	~0	14.9	~0				243
WTe_2(10)/CoTb(6)/Ta(2)	Sputtering	Magnetic loop shift			0.20							244
					2D FM							
Fe_3GeTe_2(4)/Pt(6)	Exfoliation	2ω-Hall low T	53.4	24.3								173
$Cr_2Ge_2Te_6$(19.6)/Pt(10)	Exfoliation	2ω-Hall 5 K	2.0	~0	0.25	~0						174
Fe_3GeTe_2(23)/Pt(5)	Exfoliation	2ω-Hall 180 K			0.14							175
$Cr_2Ge_2Te_6$(8)/Ta(5)	Exfoliation	Coercivity	~80									176
WTe_2(12.6)/Fe_3GeTe_2(7.3)/AlO_x(2.6)	Exfoliation	Coercivity 160 K			4.6		2.25					178
Fe_3GeTe_2(6–21)	Exfoliation	Coercivity 2 K									Anisotropy torque	210

[a] Assuming 3D carriers.
[b] Inferred from other quantities.
[c] Contribution of non-topological Rashba states included in the interpretation.
[d] Assuming 2D carriers.
[e] Reference 197 later showed that ξ^j_{DL} is largely overestimated in magnetic TIs when the asymmetric magnon scattering is disregarded in 2ω-Hall measurements.
[f] Anisotropic.

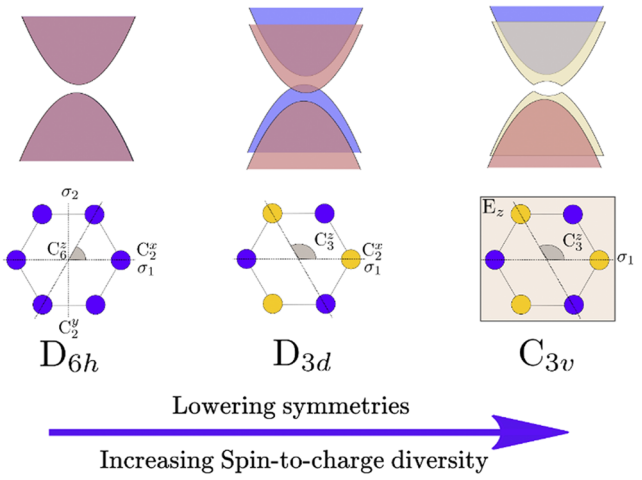

FIG. 4. Transition of the band structure and spin orientation of Dirac materials while lowering the symmetries. The quantization axis is assumed to be out-of-plane. Red and blue colors represent the bands with up and down spin. The D_{6h} point group contains 24 symmetries, including the inversion and time-reversal symmetries, which prevents spin splitting and only allows for the iSHE as the SCI mechanism due to the SOC. The D_{3d} point group contains 12 symmetries, with the inversion symmetry absent, allowing for the SHE and spin-splitting and anisotropy-like SOT. Finally, the C_{3v} point group contains six symmetries and allows for the SHE, anisotropy-like SOT, and Rashba–Edelstein effect.

and Rashba interactions on the magnetization dynamics remains to be achieved and, beyond resolving some inconsistent reports of its symmetries,[201] can lead to unprecedented features for efficient SOT applications such as zero magnetic field switching, a long sought-after mechanism for improving non-volatile memory technologies.

VI. CONCLUSIONS AND OUTLOOK

In this Perspective, we discussed the main challenges and recent results concerning materials synthesis, device fabrication, and optimization for eventually achieving the highest figures of merit for SCI in vdW heterostructures. On the material growth side, MBE is becoming an essential technique to obtain magnetic layered materials, although CVD-growth approaches and integration of two-dimensional materials in nano-electronics were already demonstrated. The next challenge is to demonstrate efficient integration of vdW materials in spintronic building blocks, such as in magnetic tunneling junctions, stimulating further research toward industry-oriented activities, for instance, in the fields of spin-transfer torque and SOT magneto-resistive random access memories. Current results concerning the SCI in vdW heterostructures combining 2D systems and topological materials are already encouraging, since they evidence high figures of merit even at room temperature in scalable materials. Besides these encouraging experimental results, advanced modeling techniques make it possible to reach a deep level of data interpretation and to predict SOT properties of arbitrary combinations of materials, even prior to their measurement, therefore acting as a pathfinder for more targeted experimental efforts. However, there are still complex theoretical issues to be tackled, such as developing very accurate effective Hamiltonian models based on first-principles. For instance, Wannier interpolation techniques, which boil down to fitting the band structure using maximally localized Wannier functions, have proven to be very accurate in realistic charge transport simulations. Nonetheless, their extension to the investigation of non-equilibrium spin properties can be problematic, as the Wannier functions do not necessarily map the crystal structure accurately. This limitation is particularly serious for SOT simulations. Indeed, the interplay between magnetism and SOC in vdW heterostructures of interest demands special care in the study of resulting ground state spin textures in the reciprocal space as well as their modification under external electric or magnetic fields. On the experimental side, current fabrication techniques demand specific material treatment to prevent rapid degradation of produced devices, which embed some materials sensitive to oxidation effects. Efforts to synthesize materials and fabricate devices *in situ* are under way, but experimental methods to produce more air-stable heterostructures are an important task to be dealt with in the near future. As a conclusion, the field of SCI in vdW heterostructures is attracting more and more attention from various scientific communities, which gives hope that progress will be achieved in the years to come in the design of ultra-compact spin devices of relevance for non-volatile technology and spin logics.

ACKNOWLEDGMENTS

The authors thank H. Okuno for the images in Figs. 2(d)–2(h). All authors acknowledge financial support from the King Abdullah University of Science and Technology under Grant No. ORS-2018-CRG7-3717. The ICN2 authors were also supported by the European Union Horizon 2020 research and innovation program under Grant Agreement Nos. 881603 (Graphene Flagship), 824140 (TOCHA, H2020-FETPROACT-01-2018), and 840588 (GRISOTO, Marie Sklodowska-Curie fellowship). ICN2 is also funded by the CERCA Programme/Generalitat de Catalunya and is supported by the Severo Ochoa program from Spanish MINECO (Grant Nos. SEV-2017-0706, PID2019-111773RB-I00/AEI/10.13039/501100011033, and RYC2019-028368-I/AEI/10.13039/501100011033). The CNRS-CEA authors acknowledge financial support from the European Union Horizon 2020 research and innovation program under Grant Agreement No. 881603 (Graphene Flagship), the French ANR projects MAGICVALLEY (Grant No. ANR-18-CE24-0007), and ELMAX (Grant No. ANR-20-CE24-0015) and from the UGA IDEX IRS/EVASPIN.

DATA AVAILABILITY

Data sharing is not applicable to this article as no new data were created or analyzed in this study.

REFERENCES

[1] A. C. Ferrari, F. Bonaccorso, V. Fal'ko, K. S. Novoselov, S. Roche, P. Bøggild, S. Borini, F. H. L. Koppens, V. Palermo, N. Pugno, J. A. Garrido, R. Sordan, A. Bianco, L. Ballerini, M. Prato, E. Lidorikis, J. Kivioja, C. Marinelli, T. Ryhänen, A. Morpurgo, J. N. Coleman, V. Nicolosi, L. Colombo, A. Fert, M. Garcia-Hernandez, A. Bachtold, G. F. Schneider, F. Guinea, C. Dekker, M. Barbone, Z. Sun, C. Galiotis, A. N. Grigorenko, G. Konstantatos, A. Kis, M. Katsnelson, L. Vandersypen, A. Loiseau, V. Morandi, D. Neumaier, E. Treossi, V. Pellegrini, M. Polini, A. Tredicucci, G. M. Williams, B. Hee Hong, J.-H. Ahn, J. Min Kim, H. Zirath, B. J. van Wees, H. van der Zant, L. Occhipinti, A. Di Matteo, I. A. Kinloch, T. Seyller,

E. Quesnel, X. Feng, K. Teo, N. Rupesinghe, P. Hakonen, S. R. T. Neil, Q. Tannock, T. Löfwander, and J. Kinaret, "Science and technology roadmap for graphene, related two-dimensional crystals, and hybrid systems," Nanoscale **7**, 4598–4810 (2015).

[2]D. Sander, S. O. Valenzuela, D. Makarov, C. H. Marrows, E. E. Fullerton, P. Fischer, J. McCord, P. Vavassori, S. Mangin, P. Pirro, B. Hillebrands, A. D. Kent, T. Jungwirth, O. Gutfleisch, C. G. Kim, and A. Berger, "The 2017 magnetism roadmap," J. Phys. D: Appl. Phys. **50**, 363001 (2017).

[3]G. R. Bhimanapati, Z. Lin, V. Meunier, Y. Jung, J. Cha, S. Das, D. Xiao, Y. Son, M. S. Strano, V. R. Cooper, L. Liang, S. G. Louie, E. Ringe, W. Zhou, S. S. Kim, R. R. Naik, B. G. Sumpter, H. Terrones, F. Xia, Y. Wang, J. Zhu, D. Akinwande, N. Alem, J. A. Schuller, R. E. Schaak, M. Terrones, and J. A. Robinson, "Recent advances in two-dimensional materials beyond graphene," ACS Nano **9**(12), 11509–11539 (2015).

[4]D. L. Duong, S. J. Yun, and Y. H. Lee, "Van der Waals layered materials: Opportunities and challenges," ACS Nano **11**, 11803–11830 (2017).

[5]G. Fiori, F. Bonaccorso, G. Iannaccone, T. Palacios, D. Neumaier, A. Seabaugh, S. K. Banerjee, and L. Colombo, "Electronics based on two-dimensional materials," Nat. Nanotechnol. **9**, 768–779 (2014).

[6]X. Xu, W. Yao, D. Xiao, and T. F. Heinz, "Spin and pseudospins in layered transition metal dichalcogenides," Nat. Phys. **10**, 343–350 (2014).

[7]D. Pesin and A. H. MacDonald, "Spintronics and pseudospintronics in graphene and topological insulators," Nat. Mater. **11**, 409–416 (2012).

[8]I. Zutic, J. Fabian, and S. Das Sarma, "Spintronics: Fundamentals and applications," Rev. Mod. Phys. **76**, 323–410 (2004).

[9]S. D. Bader and S. S. P. Parkin, "Spintronics," Annu. Rev. Condens. Matter Phys. **1**, 71–88 (2010).

[10]W. Han, R. K. Kawakami, M. Gmitra, and J. Fabian, "Graphene spintronics," Nat. Nanotechnol. **9**, 794–807 (2014).

[11]S. Roche, J. Akerman, B. Beschoten, J. C. Charlier, M. Chshiev, S. P. Dash, B. Dlubak, J. Fabian, A. Fert, M. Guimaraes, F. Guinea, I. Grigorieva, C. Schonenberger, P. Seneor, C. Stampfer, S. O. Valenzuela, X. Waintal, and B. Van Wees, "Graphene spintronics: The European Flagship perspective," 2D Mater. **2**, 030202 (2015).

[12]N. Tombros, C. Jozsa, M. Popinciuc, H. T. Jonkman, and B. J. Van Wees, "Electronic spin transport and spin precession in single graphene layers at room temperature," Nature **448**, 571–574 (2007).

[13]B. Dlubak, M.-B. Martin, C. Deranlot, B. Servet, S. Xavier, R. Mattana, M. Sprinkle, C. Berger, W. A. De Heer, F. Petroff, A. Anane, P. Seneor, and A. Fert, "Highly efficient spin transport in epitaxial graphene on SiC," Nat. Phys. **8**, 557–561 (2012).

[14]M. V. Kamalakar, C. Groenveld, A. Dankert, and S. P. Dash, "Long distance spin communication in chemical vapour deposited graphene," Nat. Commun. **6**, 6766–6773 (2015).

[15]D. Huertas-Hernando, F. Guinea, and A. Brataas, "Spin-orbit coupling in curved graphene, fullerenes, nanotubes, and nanotube caps," Phys. Rev. B **74**, 155426 (2006).

[16]N. Tombros, S. Tanabe, A. Veligura, C. Jozsa, M. Popinciuc, H. T. Jonkman, and B. J. van Wees, "Anisotropic spin relaxation in graphene," Phys. Rev. Lett. **101**(4), 046601 (2008).

[17]M. H. D. Guimarães, P. J. Zomer, J. Ingla-Aynés, J. C. Brant, N. Tombros, and B. J. van Wees, "Controlling spin relaxation in hexagonal BN-encapsulated graphene with a transverse electric field," Phys. Rev. Lett. **113**, 086602 (2014).

[18]D. V. Tuan, F. Ortmann, D. Soriano, S. O. Valenzuela, and S. Roche, "Pseudospin-driven spin relaxation mechanism in graphene," Nat. Phys. **10**, 857–863 (2014).

[19]M. Drögeler, C. Franzen, F. Volmer, T. Pohlmann, L. Banszerus, M. Wolter, K. Watanabe, T. Taniguchi, C. Stampfer, and B. Beschoten, "Spin lifetimes exceeding 12 ns in graphene nonlocal spin valve devices," Nano Lett. **16**, 3533–3539 (2016).

[20]W. Yan, L. C. Phillips, M. Barbone, S. J. Hämäläinen, A. Lombardo, M. Ghidini, X. Moya, F. MacCherozzi, S. Van Dijken, S. S. Dhesi, A. C. Ferrari, and N. D. Mathur, "Long spin diffusion length in few-layer graphene flakes," Phys. Rev. Lett. **117**, 147201 (2016).

[21]A. W. Cummings, J. H. Garcia, J. Fabian, and S. Roche, "Giant spin lifetime anisotropy in graphene induced by proximity effects," Phys. Rev. Lett. **119**, 206601 (2017).

[22]L. Yang, N. A. Sinitsyn, W. Chen, J. Yuan, J. Zhang, J. Lou, and S. A. Crooker, "Long-lived nanosecond spin relaxation and spin coherence of electrons in monolayer MoS_2 and WS_2," Nat. Phys. **11**, 830–834 (2015).

[23]P. Dey, L. Yang, C. Robert, G. Wang, B. Urbaszek, X. Marie, and S. A. Crooker, "Gate-controlled spin-valley locking of resident carriers in WSe_2 monolayers," Phys. Rev. Lett. **119**, 137401 (2017).

[24]A. Dankert, L. Langouche, M. V. Kamalakar, and S. P. Dash, "High-performance molybdenum disulfide field-effect transistors with spin tunnel contacts," ACS Nano **8**, 476–482 (2014).

[25]W. Yan, O. Txoperena, R. Llopis, H. Dery, L. E. Hueso, and F. Casanova, "A two-dimensional spin field-effect switch," Nat. Commun. **7**, 13372 (2016).

[26]A. Dankert and S. P. Dash, "Electrical gate control of spin current in van der Waals heterostructures at room temperature," Nat. Commun. **8**, 16093 (2017).

[27]V. M. Karpan, G. Giovannetti, P. A. Khomyakov, M. Talanana, A. A. Starikov, M. Zwierzycki, J. Van Den Brink, G. Brocks, and P. J. Kelly, "Graphite and graphene as perfect spin filters," Phys. Rev. Lett. **99**, 176602 (2007).

[28]A. Rycerz, J. Tworzydło, and C. W. J. Beenakker, "Valley filter and valley valve in graphene," Nat. Phys. **3**, 172–175 (2007).

[29]M.-B. Martin, B. Dlubak, R. S. Weatherup, H. Yang, C. Deranlot, K. Bouzehouane, F. Petroff, A. Anane, S. Hofmann, J. Robertson, A. Fert, and P. Seneor, "Sub-nanometer atomic layer deposition for spintronics in magnetic tunnel junctions based on graphene spin-filtering membranes," ACS Nano **8**, 7890–7895 (2014).

[30]J. Stöhr, "Exploring the microscopic origin of magnetic anisotropies with x-ray magnetic circular dichroism (XMCD) spectroscopy," J. Magn. Magn. Mater. **200**, 470–497 (1999).

[31]V. Kamberský, "Spin-orbital Gilbert damping in common magnetic metals," Phys. Rev. B **76**(13), 134416 (2007).

[32]J. Fabian, A. Matos-Abiague, C. Ertler, P. Stano, and I. Zutic, "Semiconductor spintronics," Acta Phys. Slovaca **57**(4), 565–907 (2007).

[33]J. Sinova, S. O. Valenzuela, J. Wunderlich, C. H. Back, and T. Jungwirth, "Spin Hall effect," Rev. Mod. Phys. **87**, 1213–1259 (2015).

[34]A. Hoffmann, "Spin Hall effects in metals," IEEE Trans. Magn. **49**, 5172–5193 (2013).

[35]B. A. Bernevig and O. Vafek, "Piezo-magnetoelectric effects in p-doped semiconductors," Phys. Rev. B **72**, 033203 (2005).

[36]A. Manchon and S. Zhang, "Theory of nonequilibrium intrinsic spin torque in a single nanomagnet," Phys. Rev. B **78**, 212405 (2008).

[37]L. Liu, T. Moriyama, D. C. Ralph, and R. A. Buhrman, "Spin-torque ferromagnetic resonance induced by the spin Hall effect," Phys. Rev. Lett. **106**, 036601 (2011).

[38]P. M. Haney, H.-W. Lee, K.-J. Lee, A. Manchon, and M. D. Stiles, "Current induced torques and interfacial spin-orbit coupling: Semiclassical modeling," Phys. Rev. B **87**, 174411 (2013).

[39]A. Brataas and K. M. D. Hals, "Spin-orbit torques in action," Nat. Nanotechnol. **9**, 86–88 (2014).

[40]A. Manchon and A. Belabbes, "Spin-orbitronics at transition metal interfaces," Solid State Phys. **68**, 1–89 (2017).

[41]A. Manchon, I. M. Miron, T. Jungwirth, J. Sinova, J. Zelezny, A. Thiaville, K. Garello, and P. Gambardella, "Current induced spin-orbit torques in ferromagnetic and antiferromagnetic systems," Rev. Mod. Phys. **91**, 035004 (2019).

[42]I. M. Miron, K. Garello, G. Gaudin, P.-J. Zermatten, M. V. Costache, S. Auffret, S. Bandiera, B. Rodmacq, A. Schuhl, and P. Gambardella, "Perpendicular switching of a single ferromagnetic layer induced by in-plane current injection," Nature **476**, 189–193 (2011).

[43]L. Liu, C.-F. Pai, Y. Li, H. W. Tseng, D. C. Ralph, and R. A. Buhrman, "Spin-torque switching with the giant spin Hall effect of tantalum," Science **336**, 555–558 (2012).

[44]K. Garello, C. O. Avci, I. M. Miron, M. Baumgartner, A. Ghosh, S. Auffret, O. Boulle, G. Gaudin, and P. Gambardella, "Ultrafast magnetization switching by spin-orbit torques," Appl. Phys. Lett. **105**, 212402 (2014).

[45]T. A. Gosavi, S. Manipatruni, S. V. Aradhya, G. E. Rowlands, D. Nikonov, I. A. Young, and S. A. Bhave, "Experimental demonstration of efficient spin–orbit torque switching of an MTJ with sub-100 ns pulses," IEEE Trans. Magn. **53**, 3400607 (2017).
[46]Q. H. Wang, K. Kalantar-Zadeh, A. Kis, J. N. Coleman, and M. S. Strano, "Electronics and optoelectronics of two-dimensional transition metal dichalcogenides," Nat. Nanotechnol. **7**, 699–712 (2012).
[47]D. Jariwala, V. K. Sangwan, L. J. Lauhon, T. J. Marks, and M. C. Hersam, "Emerging device applications for semiconducting two-dimensional transition metal dichalcogenides," ACS Nano **8**, 1102–1120 (2014).
[48]S. Manzeli, D. Ovchinnikov, D. Pasquier, O. V. Yazyev, and A. Kis, "2D transition metal dichalcogenides," Nat. Rev. Mater. **2**, 17033 (2017).
[49]Z. Y. Zhu, Y. C. Cheng, and U. Schwingenschlögl, "Giant spin-orbit-induced spin splitting in two-dimensional transition-metal dichalcogenide semiconductors," Phys. Rev. B **84**(15), 153402 (2011).
[50]A. K. Geim and I. V. Grigorieva, "Van der Waals heterostructures," Nature **499**, 419–425 (2013).
[51]K. S. Novoselov, A. Mishchenko, A. Carvalho, and A. H. Castro Neto, "2D materials and van der Waals heterostructures," Science **353**, aac9439 (2016).
[52]M. Gmitra and J. Fabian, "Proximity effects in bilayer graphene on monolayer WSe_2: Field-effect spin valley locking, spin-orbit valve, and spin transistor," Phys. Rev. Lett. **119**, 146401 (2017).
[53]M. M. Ugeda, A. J. Bradley, S.-F. Shi, F. H. da Jornada, Y. Zhang, D. Y. Qiu, W. Ruan, S.-K. Mo, Z. Hussain, Z.-X. Shen, F. Wang, S. G. Louie, and M. F. Crommie, "Giant bandgap renormalization and excitonic effects in a monolayer transition metal dichalcogenide semiconductor," Nat. Mater. **13**, 1091–1095 (2014).
[54]Y. J. Zhang, T. Oka, R. Suzuki, J. T. Ye, and Y. Iwasa, "Electrically switchable chiral light-emitting transistor," Science **344**, 725–730 (2014).
[55]K. F. Mak, K. He, J. Shan, and T. F. Heinz, "Control of valley polarization in monolayer MoS_2 by optical helicity," Nat. Nanotechnol. **7**, 494–498 (2012).
[56]H. Zeng, J. Dai, W. Yao, D. Xiao, and X. Cui, "Valley polarization in MoS_2 monolayers by optical pumping," Nat. Nanotechnol. **7**(8), 490–493 (2012).
[57]S. Wu, J. S. Ross, G.-B. Liu, G. Aivazian, A. Jones, Z. Fei, W. Zhu, D. Xiao, W. Yao, D. Cobden, and X. Xu, "Electrical tuning of valley magnetic moment through symmetry control in bilayer MoS_2," Nat. Phys. **9**, 149–153 (2013).
[58]R. Suzuki, M. Sakano, Y. J. Zhang, R. Akashi, D. Morikawa, A. Harasawa, K. Yaji, K. Kuroda, K. Miyamoto, T. Okuda, K. Ishizaka, R. Arita, and Y. Iwasa, "Valley-dependent spin polarization in bulk MoS_2 with broken inversion symmetry," Nat. Nanotechnol. **9**, 611–617 (2014).
[59]K. F. Mak, K. L. McGill, J. Park, and P. L. McEuen, "The valley Hall effect in MoS_2 transistors," Science **344**, 1489–1492 (2014).
[60]H. Yuan, X. Wang, B. Lian, H. Zhang, X. Fang, B. Shen, G. Xu, Y. Xu, S.-C. Zhang, H. Y. Hwang, and Y. Cui, "Generation and electric control of spin-valley-coupled circular photogalvanic current in WSe_2," Nat. Nanotechnol. **9**, 851–857 (2014).
[61]K. Deng, G. Wan, P. Deng, K. Zhang, S. Ding, E. Wang, M. Yan, H. Huang, H. Zhang, Z. Xu, J. Denlinger, A. Fedorov, H. Yang, W. Duan, H. Yao, Y. Wu, S. Fan, H. Zhang, X. Chen, and S. Zhou, "Experimental observation of topological Fermi arcs in type-II Weyl semimetal $MoTe_2$," Nat. Phys. **12**, 1105–1110 (2016).
[62]L. Huang, T. M. McCormick, M. Ochi, Z. Zhao, M.-T. Suzuki, R. Arita, Y. Wu, D. Mou, H. Cao, J. Yan, N. Trivedi, and A. Kaminski, "Spectroscopic evidence for a type II Weyl semimetallic state in $MoTe_2$," Nat. Mater. **15**, 1155–1160 (2016).
[63]A. Tamai, Q. S. Wu, I. Cucchi, F. Y. Bruno, S. Riccò, T. K. Kim, M. Hoesch, C. Barreteau, E. Giannini, C. Besnard, A. A. Soluyanov, and F. Baumberger, "Fermi arcs and their topological character in the candidate type-II Weyl semimetal $MoTe_2$," Phys. Rev. X **6**, 031021 (2016).
[64]J. M. Lu, O. Zheliuk, I. Leermakers, N. F. Q. Yuan, U. Zeitler, K. T. Law, and J. T. Ye, "Evidence for two-dimensional Ising superconductivity in gated MoS_2," Science **350**, 1353–1357 (2015).
[65]X. Xi, Z. Wang, W. Zhao, J.-H. Park, K. T. Law, H. Berger, L. Forró, J. Shan, and K. F. Mak, "Ising pairing in superconducting $NbSe_2$ atomic layers," Nat. Phys. **12**, 139–143 (2016).
[66]M. Bonilla, S. Kolekar, Y. Ma, H. C. Diaz, V. Kalappattil, R. Das, T. Eggers, H. R. Gutierrez, M.-H. Phan, and M. Batzill, "Strong room-temperature ferromagnetism in VSe_2 monolayers on van der Waals substrates," Nat. Nanotechnol. **13**, 289–293 (2018).
[67]M. Z. Hasan and J. E. Moore, "Three-dimensional topological insulators," Annu. Rev. Condens. Matter Phys. **2**, 55–78 (2011).
[68]F. Ortmann, S. Roche, and S. O. Valenzuela, *Topological Insulators* (Wiley-VCH, Weinheim, 2015).
[69]A. R. Mellnik, J. S. Lee, A. Richardella, J. L. Grab, P. J. Mintun, M. H. Fischer, A. Vaezi, A. Manchon, E.-A. Kim, N. Samarth, and D. C. Ralph, "Spin-transfer torque generated by a topological insulator," Nature **511**, 449–451 (2014).
[70]Y. Wang, P. Deorani, K. Banerjee, N. Koirala, M. Brahlek, S. Oh, and H. Yang, "Topological surface states originated spin–orbit torques in Bi_2Se_3," Phys. Rev. Lett. **114**, 257202 (2015).
[71]J. Han, A. Richardella, S. A. Siddiqui, J. Finley, N. Samarth, and L. Liu, "Room-temperature spin–orbit torque switching induced by a topological insulator," Phys. Rev. Lett. **119**, 077702 (2017).
[72]Y. Wang, D. Zhu, Y. Wu, Y. Yang, J. Yu, R. Ramaswamy, R. Mishra, S. Shi, M. Elyasi, K.-L. Teo, Y. Wu, and H. Yang, "Room temperature magnetization switching in topological insulator-ferromagnet heterostructures by spin-orbit torques," Nat. Commun. **8**, 1364 (2017).
[73]D. C. Mahendra, R. Grassi, J.-Y. Chen, M. Jamali, D. Reifsnyder Hickey, D. Zhang, Z. Zhao, H. Li, P. Quarterman, Y. Lv, M. Li, A. Manchon, K. A. Mkhoyan, T. Low, and J.-P. Wang, "Room temperature giant spin–orbit torque due to quantum confinement in sputtered $Bi_xSe_{(1-x)}$ films," Nat. Mater. **17**, 800–807 (2018).
[74]Q. Shao, G. Yu, Y.-W. Lan, Y. Shi, M.-Y. Li, C. Zheng, X. Zhu, L.-J. Li, P. K. Amiri, and K. L. Wang, "Strong Rashba–Edelstein effect-induced spin-orbit torques in monolayer transition metal dichalcogenide/ferromagnet bilayers," Nano Lett. **16**, 7514–7520 (2016).
[75]C. Cheng, M. Collet, J.-C. Rojas Sánchez, V. Ivanovskaya, B. Dlubak, P. Seneor, A. Fert, H. Kim, G. H. Han, Y. H. Lee, H. Yang, and A. Anane, "Spin to charge conversion in MoS_2 monolayer with spin pumping," arXiv:1510.03451 (2016).
[76]Y. Huang, Y.-H. Pan, R. Yang, L.-H. Bao, L. Meng, H.-L. Luo, Y.-Q. Cai, G.-D. Liu, W.-J. Zhao, Z. Zhou, L.-M. Wu, Z.-L. Zhu, M. Huang, L.-W. Liu, L. Liu, P. Cheng, K.-H. Wu, S.-B. Tian, C.-Z. Gu, Y.-G. Shi, Y.-F. Guo, Z. G. Cheng, J.-P. Hu, L. Zhao, G.-H. Yang, E. Sutter, P. Sutter, Y.-L. Wang, W. Ji, X.-J. Zhou, and H.-J. Gao, "Universal mechanical exfoliation of large-area 2D crystals," Nat. Commun. **11**, 2453 (2020).
[77]X. Li, W. Cai, J. An, S. Kim, J. Nah, D. Yang, R. Piner, A. Velamakanni, I. Jung, E. Tutuc, S. K. Banerjee, L. Colombo, and R. S. Ruoff, "Large-area synthesis of high-quality and uniform graphene films on copper foils," Science **324**, 1312–1314 (2009).
[78]Y. Zhang, Y. Yao, M. G. Sendeku, L. Yin, X. Zhan, F. Wang, Z. Wang, and J. He, "Recent progress in CVD growth of 2D transition metal dichalcogenides and related heterostructures," Adv. Mater. **31**, 1901694 (2019).
[79]X. Xu, Z. Zhang, L. Qiu, J. Zhuang, L. Zhang, H. Wang, C. Liao, H. Song, R. Qiao, P. Gao, Z. Hu, L. Liao, Z. Liao, D. Yu, E. Wang, F. Ding, H. Peng, and K. Liu, "Ultrafast growth of single-crystal graphene assisted by a continuous oxygen supply," Nat. Nanotechnol. **11**, 930–935 (2016).
[80]B. Deng, Z. Liu, and H. Peng, "Toward mass production of CVD graphene films," Adv. Mater. **31**, 1800996 (2019).
[81]M. Chen, J. Li, J. Zhang, Y. Ma, H. Dong, W. Li, E. Bekyarova, Y. F. Al-Hadeethi, L. Chen, M. N. Hedhili, B. Tian, and X. Zhang, "Evolution of cellulose acetate to monolayer graphene," Carbon **174**, 24–35 (2021).
[82]A. Ismach, C. Druzgalski, S. Penwell, A. Schwartzberg, M. Zheng, A. Javey, J. Bokor, and Y. Zhang, "Direct chemical vapor deposition of graphene on dielectric surfaces," Nano Lett. **10**, 1542–1548 (2010).
[83]P. Zhuang, W. Lin, B. Tian, C. Zhang, Z. Zhao, T.-M. Shih, and W. Cai, "Atomic-concentration diffusion governing integrated-territory graphene syntheses at catalyst–insulator interfaces," Carbon **102**, 403–408 (2016).
[84]S. Xu, L. Zhang, B. Wang, and R. S. Ruoff, "Chemical vapor deposition of graphene on thin-metal films," Cell Rep. Phys. Sci. **2**, 100372 (2021).
[85]B. Guo, L. Fang, B. Zhang, and J. R. Gong, "Graphene doping: A review," Insci. J. **1**, 80–89 (2011).

[86]H. Liu, Y. Liu, and D. Zhu, "Chemical doping of graphene," J. Mater. Chem. **21**, 3335–3345 (2011).
[87]W. Lin, B. Tian, P. Zhuang, J. Yin, C. Zhang, Q. Li, T.-m. Shih, and W. Cai, "Graphene-based fluorescence-quenching-related Fermi level elevation and electron-concentration surge," Nano Lett. **16**, 5737–5741 (2016).
[88]X. Liang, B. A. Sperling, I. Calizo, G. Cheng, C. A. Hacker, Q. Zhang, Y. Obeng, K. Yan, H. Peng, Q. Li, X. Zhu, H. Yuan, A. R. Hight Walker, Z. Liu, L.-m. Peng, and C. A. Richter, "Toward clean and crackless transfer of graphene," ACS Nano **5**, 9144–9153 (2011).
[89]J. Kang, D. Shin, S. Bae, and B. H. Hong, "Graphene transfer: Key for applications," Nanoscale **4**, 5527–5537 (2012).
[90]W. S. Leong, H. Wang, J. Yeo, F. J. Martin-Martinez, A. Zubair, P.-C. Shen, Y. Mao, T. Palacios, M. J. Buehler, J.-Y. Hong, and J. Kong, "Paraffin-enabled graphene transfer," Nat. Commun. **10**, 867 (2019).
[91]D. Geng, H. Wang, and G. Yu, "Graphene single crystals: Size and morphology engineering," Adv. Mater. **27**, 2821–2837 (2015).
[92]J. Li, M. Chen, C. Zhang, H. Dong, W. Lin, P. Zhuang, Y. Wen, B. Tian, W. Cai, and X. Zhang, "Fractal-theory-based control of the shape and quality of CVD-grown 2D materials," Adv. Mater. **31**, 1902431 (2019).
[93]H. Wang, X. Xue, Q. Jiang, Y. Wang, D. Geng, L. Cai, L. Wang, Z. Xu, and G. Yu, "Primary nucleation-dominated chemical vapor deposition growth for uniform graphene monolayers on dielectric substrate," J. Am. Chem. Soc. **141**, 11004–11008 (2019).
[94]Y. Cao, V. Fatemi, A. Demir, S. Fang, S. L. Tomarken, J. Y. Luo, J. D. Sanchez-Yamagishi, K. Watanabe, T. Taniguchi, E. Kaxiras, R. C. Ashoori, and P. Jarillo-Herrero, "Correlated insulator behaviour at half-filling in magic-angle graphene superlattices," Nature **556**, 80–84 (2018).
[95]Y. Cao, V. Fatemi, S. Fang, K. Watanabe, T. Taniguchi, E. Kaxiras, and P. Jarillo-Herrero, "Unconventional superconductivity in magic-angle graphene superlattices," Nature **556**, 43–50 (2018).
[96]Y. Cao, D. Rodan-Legrain, O. Rubies-Bigorda, J. M. Park, K. Watanabe, T. Taniguchi, and P. Jarillo-Herrero, "Tunable correlated states and spin-polarized phases in twisted bilayer-bilayer graphene," Nature **583**, 215–220 (2020).
[97]D. Luo, M. Wang, Y. Li, C. Kim, K. M. Yu, Y. Kim, H. Han, M. Biswal, M. Huang, Y. Kwon, M. Goo, D. C. Camacho-Mojica, H. Shi, W. J. Yoo, M. S. Altman, H. J. Shin, and R. S. Ruoff, "Adlayer-free large-area single crystal graphene grown on a Cu(111) foil," Adv. Mater. **31**, 1903615 (2019).
[98]S. Jin, M. Huang, Y. Kwon, L. Zhang, B.-W. Li, S. Oh, J. Dong, D. Luo, M. Biswal, B. V. Cunning, P. V. Bakharev, I. Moon, W. J. Yoo, D. C. Camacho-Mojica, Y.-J. Kim, S. H. Lee, B. Wang, W. K. Seong, M. Saxena, F. Ding, H.-J. Shin, and R. S. Ruoff, "Colossal grain growth yields single-crystal metal foils by contact-free annealing," Science **362**, 1021–1025 (2018).
[99]Y. Liu, S. Bhowmick, and B. I. Yakobson, "BN white graphene with 'colorful' edges: The energies and morphology," Nano Lett. **11**, 3113–3116 (2011).
[100]Z. Yan, Z. Peng, Z. Sun, J. Yao, Y. Zhu, Z. Liu, P. M. Ajayan, and J. M. Tour, "Growth of bilayer graphene on insulating substrates," ACS Nano **5**, 8187–8192 (2011).
[101]H. Dong, J. Li, M. Chen, H. Wang, X. Jiang, Y. Xiao, B. Tian, and X. Zhang, "High-throughput production of ZnO-MoS_2-graphene heterostructures for highly efficient photocatalytic hydrogen evolution," Materials **12**, 2233–2244 (2019).
[102]T.-A. Chen, C.-P. Chuu, C.-C. Tseng, C.-K. Wen, H.-S. P. Wong, S. Pan, R. Li, T.-A. Chao, W.-C. Chueh, Y. Zhang, Q. Fu, B. I. Yakobson, W.-H. Chang, and L.-J. Li, "Wafer-scale single-crystal hexagonal boron nitride monolayers on Cu (111)," Nature **579**, 219–223 (2020).
[103]C. Muratore, A. A. Voevodin, and N. R. Glavin, "Physical vapor deposition of 2D Van der Waals materials: A review," Thin Solid Films **688**, 137500 (2019).
[104]T. Chowdhury, E. C. Sadler, and T. J. Kempa, "Progress and prospects in transition-metal dichalcogenide research beyond 2D," Chem. Rev. **120**, 12563–12591 (2020).
[105]S. Najmaei, Z. Liu, W. Zhou, X. Zou, G. Shi, S. Lei, B. I. Yakobson, J.-C. Idrobo, P. M. Ajayan, and J. Lou, "Vapour phase growth and grain boundary structure of molybdenum disulphide atomic layers," Nat. Mater. **12**, 754–759 (2013).
[106]Q. Ji, Y. Zhang, T. Gao, Y. Zhang, D. Ma, M. Liu, Y. Chen, X. Qiao, P.-H. Tan, M. Kan, J. Feng, Q. Sun, and Z. Liu, "Epitaxial monolayer MoS_2 on mica with novel photoluminescence," Nano Lett. **13**, 3870–3877 (2013).
[107]H. Yu, M. Liao, W. Zhao, G. Liu, X. J. Zhou, Z. Wei, X. Xu, K. Liu, Z. Hu, K. Deng, S. Zhou, J.-A. Shi, L. Gu, C. Shen, T. Zhang, L. Du, L. Xie, J. Zhu, W. Chen, R. Yang, D. Shi, and G. Zhang, "Wafer-scale growth and transfer of highly-oriented monolayer MoS_2 continuous films," ACS Nano **11**, 12001–12007 (2017).
[108]X. Lu, M. I. B. Utama, J. Lin, X. Gong, J. Zhang, Y. Zhao, S. T. Pantelides, J. Wang, Z. Dong, Z. Liu, W. Zhou, and Q. Xiong, "Large-area synthesis of monolayer and few-layer $MoSe_2$ films on SiO_2 substrates," Nano Lett. **14**, 2419–2425 (2014).
[109]Y.-H. Chang, W. Zhang, Y. Zhu, Y. Han, J. Pu, J.-K. Chang, W.-T. Hsu, J.-K. Huang, C.-L. Hsu, M.-H. Chiu, T. Takenobu, H. Li, C.-I. Wu, W.-H. Chang, A. T. S. Wee, and L.-J. Li, "Monolayer $MoSe_2$ grown by chemical vapor deposition for fast photodetection," ACS Nano **8**, 8582–8590 (2014).
[110]M. Kim, J. Seo, J. Kim, J. S. Moon, J. Lee, J.-H. Kim, J. Kang, and H. Park, "High-crystalline monolayer transition metal dichalcogenides films for wafer-scale electronics," ACS Nano **15**, 3038–3046 (2021).
[111]Z. Jia, J. Dong, L. Liu, J. Xiang, A. Nie, F. Wen, C. Mu, B. Wang, K. Zhai, Z. Yu, M. Kang, and Z. Liu, "One-step growth of wafer-scale monolayer tungsten disulfide via hydrogen sulfide assisted chemical vapor deposition," Appl. Phys. Lett. **115**, 163104 (2019).
[112]J. Li, X. Yang, Y. Liu, B. Huang, R. Wu, Z. Zhang, B. Zhao, H. Ma, W. Dang, Z. Wei, K. Wang, Z. Lin, X. Yan, M. Sun, B. Li, X. Pan, J. Luo, G. Zhang, Y. Liu, Y. Huang, X. Duan, and X. Duan, "General synthesis of two-dimensional van der Waals heterostructure arrays," Nature **579**, 368–374 (2020).
[113]V. V. Kulish and W. Huang, "Single-layer metal halides MX_2 (X = Cl, Br, I): Stability and tunable magnetism from first principles and Monte Carlo simulations," J. Mater. Chem. C **5**, 8734–8741 (2017).
[114]Y. Guo, L. Kang, S. Yu, J. Yang, X. Qi, Z. Zhang, and Z. Liu, "CVD growth of large-scale and highly crystalline 2D chromium telluride nanoflakes," ChemNanoMat **7**, 323–327 (2021).
[115]M. Mogi, T. Nakajima, V. Ukleev, A. Tsukazaki, R. Yoshimi, M. Kawamura, K. S. Takahashi, T. Hanashima, K. Kakurai, T. Arima, M. Kawasaki, and Y. Tokura, "Large anomalous Hall effect in topological insulators with proximitized ferromagnetic insulators," Phys. Rev. Lett. **123**, 016804 (2019).
[116]A. Koma, "Van der Waals epitaxy—A new epitaxial growth method for a highly lattice-mismatched system," Thin Solid Films **216**, 72–76 (1992).
[117]G. Zhang, H. Qin, J. Chen, X. He, L. Lu, Y. Li, and K. Wu, "Growth of topological insulator Bi_2Se_3 thin films on $SrTiO_3$ with large tunability in chemical potential," Adv. Funct. Mater. **21**, 2351–2355 (2011).
[118]N. V. Tarakina, S. Schreyeck, M. Luysberg, S. Grauer, C. Schumacher, G. Karczewski, K. Brunner, C. Gould, H. Buhmann, R. E. Dunin-Borkowski, and L. W. Molenkamp, "Suppressing twin formation in Bi_2Se_3 thin films," Adv. Mater. Interfaces **1**, 1400134 (2014).
[119]R. Yoshimi, K. Yasuda, A. Tsukazaki, K. S. Takahashi, N. Nagaosa, M. Kawasaki, and Y. Tokura, "Quantum Hall states stabilized in semi-magnetic bilayers of topological insulators," Nat. Commun. **6**, 8530 (2015).
[120]A. Richardella, A. Kandala, J. S. Lee, and N. Samarth, "Characterizing the structure of topological insulator thin films," APL Mater. **3**, 083303 (2015).
[121]J. Kampmeier, S. Borisova, L. Plucinski, M. Luysberg, G. Mussler, and D. Grützmacher, "Suppressing twin domains in molecular beam epitaxy grown Bi_2Te_3 topological insulator thin films," Cryst. Growth Des. **15**, 390–394 (2015).
[122]F. Bonell, M. G. Cuxart, K. Song, R. Robles, P. Ordejón, S. Roche, A. Mugarza, and S. O. Valenzuela, "Growth of twin-free and low-doped topological insulators on BaF_2(111)," Cryst. Growth Des. **17**, 4655–4660 (2017).
[123]T. Guillet, A. Marty, C. Beigné, C. Vergnaud, M.-T. Dau, P. Noël, J. Frigerio, G. Isella, and M. Jamet, "Magnetotransport in Bi_2Se_3 thin films epitaxially grown on Ge(111)," AIP Adv. **8**, 115125 (2018).
[124]J. S. Lee, A. Richardella, R. D. Fraleigh, C.-X. Liu, W. Zhao, and N. Samarth, "Engineering the breaking of time-reversal symmetry in gate-tunable hybrid ferromagnet/topological insulator heterostructures," npj Quantum Mater. **3**, 51–57 (2018).

[125]C.-Z. Chang, J. Zhang, X. Feng, J. Shen, Z. Zhang, M. Guo, K. Li, Y. Ou, P. Wei, L.-L. Wang, Z.-Q. Ji, Y. Feng, S. Ji, X. Chen, J. Jia, X. Dai, Z. Fang, S.-C. Zhang, K. He, Y. Wang, L. Lu, X.-C. Ma, and Q.-K. Xue, "Experimental observation of the quantum anomalous Hall effect in a magnetic topological insulator," Science **340**, 167–170 (2013).
[126]C.-Z. Chang, W. Zhao, D. Y. Kim, H. Zhang, B. A. Assaf, D. Heiman, S.-C. Zhang, C. Liu, M. H. W. Chan, and J. S. Moodera, "High-precision realization of robust quantum anomalous Hall state in a hard ferromagnetic topological insulator," Nat. Mater. **14**, 473–477 (2015).
[127]M. Mogi, R. Yoshimi, A. Tsukazaki, K. Yasuda, Y. Kozuka, K. S. Takahashi, M. Kawasaki, and Y. Tokura, "Magnetic modulation doping in topological insulators toward higher-temperature quantum anomalous Hall effect," Appl. Phys. Lett. **107**, 182401 (2015).
[128]M. Winnerlein, S. Schreyeck, S. Grauer, S. Rosenberger, K. M. Fijalkowski, C. Gould, K. Brunner, and L. W. Molenkamp, "Epitaxy and structural properties of $(V, Bi, Sb)_2Te_3$ layers exhibiting the quantum anomalous Hall effect," Phys. Rev. Mater. **1**, 011201(R) (2017).
[129]T. Hirahara, S. V. Eremeev, T. Shirasawa, Y. Okuyama, T. Kubo, R. Nakanishi, R. Akiyama, A. Takayama, T. Hajiri, S.-I. Ideta, M. Matsunami, K. Sumida, K. Miyamoto, Y. Takagi, K. Tanaka, T. Okuda, T. Yokoyama, S.-I. Kimura, S. Hasegawa, and E. V. Chulkov, "Large-gap magnetic topological heterostructure formed by subsurface incorporation of a ferromagnetic layer," Nano Lett. **17**, 3493–3500 (2017).
[130]C. Nowka, M. Gellesch, J. Enrique Hamann Borrero, S. Partzsch, C. Wuttke, F. Steckel, C. Hess, A. U. B. Wolter, L. Teresa Corredor Bohorquez, B. Büchner, and S. Hampel, "Chemical vapor transport and characterization of $MnBi_2Se_4$," J. Cryst. Growth **459**, 81–86 (2017).
[131]Y. Gong, J. Guo, J. Li, K. Zhu, M. Liao, X. Liu, Q. Zhang, L. Gu, L. Tang, X. Feng, D. Zhang, W. Li, C. Song, L. Wang, P. Yu, X. Chen, Y. Wang, H. Yao, W. Duan, Y. Xu, S.-C. Zhang, X. Ma, Q.-K. Xue, and K. He, "Experimental realization of an intrinsic magnetic topological insulator," Chin. Phys. Lett. **36**, 076801 (2019).
[132]P. Kagerer, C. I. Fornari, S. Buchberger, S. L. Morelhão, R. C. Vidal, A. Tcakaev, V. Zabolotnyy, E. Weschke, V. Hinkov, M. Kamp, B. Büchner, A. Isaeva, H. Bentmann, and F. Reinert, "Molecular beam epitaxy of antiferromagnetic $(MnBi_2Te_4)(Bi_2Te_3)$ thin films on $BaF_2(111)$," J. Appl. Phys. **128**, 135303 (2020).
[133]A. I. Figueroa, T. Hesjedal, and N.-J. Steinke, "Magnetic order in 3D topological insulators–Wishful thinking or gateway to emergent quantum effects?," Appl. Phys. Lett. **117**, 150502 (2020).
[134]Z. Liao, M. Brahlek, J. Mok Ok, L. Nuckols, Y. Sharma, Q. Lu, Y. Zhang, and H. Nyung Lee, "Pulsed-laser epitaxy of topological insulator Bi2Te3 thin films," APL Mater. **7**, 041101 (2019).
[135]Y. Zhang, T.-R. Chang, B. Zhou, Y.-T. Cui, H. Yan, Z. Liu, F. Schmitt, J. Lee, R. Moore, Y. Chen, H. Lin, H.-T. Jeng, S.-K. Mo, Z. Hussain, A. Bansil, and Z.-X. Shen, "Direct observation of the transition from indirect to direct bandgap in atomically thin epitaxial $MoSe_2$," Nat. Nanotechnol. **9**, 111–115 (2014).
[136]H. C. Diaz, R. Chaghi, Y. Ma, and M. Batzill, "Molecular beam epitaxy of the van der Waals heterostructure $MoTe_2$ on MoS_2: Phase, thermal, and chemical stability," 2D Mater. **2**, 044010 (2015).
[137]E. Xenogiannopoulou, P. Tsipas, K. E. Aretouli, D. Tsoutsou, S. A. Giamini, C. Bazioti, G. P. Dimitrakopulos, P. Komninou, S. Brems, C. Huyghebaert, I. P. Radu, and A. Dimoulas, "High-quality, large-area $MoSe_2$ and $MoSe_2/Bi_2Se_3$ heterostructures on AlN(0001)/Si(111) substrates by molecular beam epitaxy," Nanoscale **7**, 7896–7905 (2015).
[138]R. Yue, Y. Nie, L. A. Walsh, R. Addou, C. Liang, N. Lu, A. T. Barton, H. Zhu, Z. Che, D. Barrera, L. Cheng, P.-R. Cha, Y. J. Chabal, J. W. P. Hsu, J. Kim, M. J. Kim, L. Colombo, R. M. Wallace, K. Cho, and C. L. Hinkle, "Nucleation and growth of WSe_2: Enabling large grain transition metal dichalcogenides," 2D Mater. **4**, 045019 (2017).
[139]K. E. Aretouli, P. Tsipas, D. Tsoutsou, J. Marquez-Velasco, E. Xenogiannopoulou, S. A. Giamini, E. Vassalou, N. Kelaidis, and A. Dimoulas, "Two-dimensional semiconductor $HfSe_2$ and $MoSe_2/HfSe_2$ van der Waals heterostructures by molecular beam epitaxy," Appl. Phys. Lett. **106**, 143105 (2015).
[140]M. M. Ugeda, A. J. Bradley, Y. Zhang, S. Onishi, Y. Chen, W. Ruan, C. Ojeda-Aristizabal, H. Ryu, M. T. Edmonds, H.-Z. Tsai, A. Riss, S.-K. Mo, D. Lee, A. Zettl, Z. Hussain, Z.-X. Shen, and M. F. Crommie, "Characterization of collective ground states in single-layer $NbSe_2$," Nat. Phys. **12**, 92–97 (2016).
[141]S. Vishwanath, X. Liu, S. Rouvimov, L. Basile, N. Lu, A. Azcatl, K. Magno, R. M. Wallace, M. Kim, J.-C. Idrobo, J. K. Furdyna, D. Jena, and H. G. Xing, "Controllable growth of layered selenide and telluride heterostructures and superlattices using molecular beam epitaxy," J. Mater. Res. **31**, 900–910 (2016).
[142]M.-W. Chen, D. Ovchinnikov, S. Lazar, M. Pizzochero, M. B. Whitwick, A. Surrente, M. Baranowski, O. L. Sanchez, P. Gillet, P. Plochocka, O. V. Yazyev, and A. Kis, "Highly oriented atomically thin ambipolar $MoSe_2$ grown by molecular beam epitaxy," ACS Nano **11**, 6355–6361 (2017).
[143]M. Nakano, Y. Wang, Y. Kashiwabara, H. Matsuoka, and Y. Iwasa, "Layer-by-layer epitaxial growth of scalable WSe_2 on sapphire by molecular beam epitaxy," Nano Lett. **17**, 5595–5599 (2017).
[144]L. A. Walsh, R. Yue, Q. Wang, A. T. Barton, R. Addou, C. M. Smyth, H. Zhu, J. Kim, L. Colombo, M. J. Kim, R. M. Wallace, and C. L. Hinkle, "WTe_2 thin films grown by beam-interrupted molecular beam epitaxy," 2D Mater. **4**, 025044 (2017).
[145]M. Yan, E. Wang, X. Zhou, G. Zhang, H. Zhang, K. Zhang, W. Yao, N. Lu, S. Yang, S. Wu, T. Yoshikawa, K. Miyamoto, T. Okuda, Y. Wu, P. Yu, W. Duan, and S. Zhou, "High quality atomically thin $PtSe_2$ films grown by molecular beam epitaxy," 2D Mater. **4**, 045015 (2017).
[146]P. Tsipas, D. Tsoutsou, S. Fragkos, R. Sant, C. Alvarez, H. Okuno, G. Renaud, R. Alcotte, T. Baron, and A. Dimoulas, "Massless Dirac fermions in $ZrTe_2$ semimetal grown on InAs(111) by van der Waals epitaxy," ACS Nano **12**, 1696–1703 (2018).
[147]M. T. Dau, M. Gay, D. Di Felice, C. Vergnaud, A. Marty, C. Beigné, G. Renaud, O. Renault, P. Mallet, T. Le Quang, J.-Y. Veuillen, L. Huder, V. T. Renard, C. Chapelier, G. Zamborlini, M. Jugovac, V. Feyer, Y. J. Dappe, P. Pochet, and M. Jamet, "Beyond van der Waals interaction: The case of $MoSe_2$ epitaxially grown on few-layer graphene," ACS Nano **12**, 2319–2331 (2018).
[148]M. T. Dau, C. Vergnaud, A. Marty, C. Beigné, S. Gambarelli, V. Maurel, T. Journot, B. Hyot, T. Guillet, B. Grévin, H. Okuno, and M. Jamet, "The valley Nernst effect in WSe_2," Nat. Commun. **10**, 5796 (2019).
[149]C. Vergnaud, M.-T. Dau, B. Grévin, C. Licitra, A. Marty, H. Okuno, and M. Jamet, "New approach for the molecular beam epitaxy growth of scalable WSe_2 monolayers," Nanotechnol **31**, 255602 (2020).
[150]W. Chen, M. Hu, J. Zong, X. Xie, Q. Meng, F. Yu, L. Wang, W. Ren, A. Chen, G. Liu, X. Xi, F. S. Li, J. Sun, J. Liu, and Y. Zhang, "Epitaxial growth of single-phase $1T'$-WSe_2 monolayer with assistance of enhanced interface interaction," Adv. Mater. **33**, 2004930 (2020).
[151]H. Li, A. Chen, L. Wang, W. Ren, S. Lu, B. Yang, Y.-P. Jiang, and F.-S. Li, "Molecular beam epitaxy growth and strain-induced bandgap of monolayer $1T'$-WTe_2 on $SrTiO_3(001)$," Appl. Phys. Lett. **117**, 161601 (2020).
[152]S. J. Yun, D. L. Duong, D. M. Ha, K. Singh, T. L. Phan, W. Choi, Y. M. Kim, and Y. H. Lee, "Ferromagnetic order at room temperature in monolayer WSe_2 semiconductor via vanadium dopant," Adv. Sci. **7**, 1903076 (2020).
[153]P. Mallet, F. Chiapello, H. Okuno, H. Boukari, M. Jamet, and J.-Y. Veuillen, "Bound hole states associated to individual vanadium atoms incorporated into monolayer WSe_2," Phys. Rev. Lett. **125**, 036802 (2020).
[154]M. T. Dau, C. Vergnaud, M. Gay, C. J. Alvarez, A. Marty, C. Beigné, D. Jalabert, J.-F. Jacquot, O. Renault, H. Okuno, and M. Jamet, "Van der Waals epitaxy of Mn-doped $MoSe_2$ on mica," APL Mater. **7**, 051111 (2019).
[155]C. Vergnaud, M. Gay, C. Alvarez, M.-T. Dau, F. Pierre, D. Jalabert, C. Licitra, A. Marty, C. Beigné, B. Grévin, O. Renault, H. Okuno, and M. Jamet, "Van der Waals solid phase epitaxy to grow large-area manganese-doped MoSe2 few-layers on SiO_2/Si," 2D Mater. **6**, 035019 (2019).
[156]M. Nakano, Y. Wang, S. Yoshida, H. Matsuoka, Y. Majima, K. Ikeda, Y. Hirata, Y. Takeda, H. Wadati, Y. Kohama, Y. Ohigashi, M. Sakano, K. Ishizaka, and Y. Iwasa, "Intrinsic 2D ferromagnetism in V_5Se_8 epitaxial thin films," Nano Lett. **19**, 8806–8810 (2019).
[157]Y. Fujisawa, M. Pardo-Almanza, J. Garland, K. Yamagami, X. Zhu, X. Chen, K. Araki, T. Takeda, M. Kobayashi, Y. Takeda, C. H. Hsu, F. C. Chuang, R. Laskowski, K. H. Khoo, A. Soumyanarayanan, and Y. Okada, "Tailoring magnetism in self-intercalated $Cr_{1+\delta}Te_2$ epitaxial films," Phys. Rev. Mater. **4**, 114001 (2020).
[158]M. Mogi, A. Tsukazaki, Y. Kaneko, R. Yoshimi, K. S. Takahashi, M. Kawasaki, and Y. Tokura, "Ferromagnetic insulator $Cr_2Ge_2Te_6$ thin films with perpendicular remanence," APL Mater. **6**, 091104 (2018).

[159]S. Liu, X. Yuan, Y. Zou, Y. Sheng, C. Huang, E. Zhang, J. Ling, Y. Liu, W. Wang, C. Zhang, J. Zou, K. Wang, and F. Xiu, "Wafer-scale two-dimensional ferromagnetic Fe_3GeTe_2 thin films grown by molecular beam epitaxy," npj 2D Mater. Appl. **1**, 30–36 (2017).
[160]R. Roemer, C. Liu, and K. Zou, "Robust ferromagnetism in wafer-scale monolayer and multilayer Fe_3GeTe_2," npj 2D Mater. Appl. **4**, 33–39 (2020).
[161]H. Wang, Y. Liu, P. Wu, W. Hou, Y. Jiang, X. Li, C. Pandey, D. Chen, Q. Yang, H. Wang, D. Wei, N. Lei, W. Kang, L. Wen, T. Nie, W. Zhao, and K. L. Wang, "Above room-temperature ferromagnetism in wafer-scale two-dimensional van der Waals Fe_3GeTe_2 tailored by a topological insulator," ACS Nano **14**, 10045–10053 (2020).
[162]M. Kim, P. Kumaravadivel, J. Birkbeck, W. Kuang, S. G. Xu, D. G. Hopkinson, J. Knolle, P. A. McClarty, A. I. Berdyugin, M. Ben Shalom, R. V. Gorbachev, S. J. Haigh, S. Liu, J. H. Edgar, K. S. Novoselov, I. V. Grigorieva, and A. K. Geim, "Micromagnetometry of two-dimensional ferromagnets," Nat. Electron. **2**, 457–463 (2019).
[163]A. Bedoya-Pinto, J.-R. Ji, A. Pandeya, P. Gargiani, M. Valvidares, P. Sessi, F. Radu, K. Chang, and S. Parkin, "Intrinsic 2D-XY ferromagnetism in a van der Waals monolayer," arXiv:2006.07605 (2020).
[164]P. Li, C. Wang, J. Zhang, S. Chen, D. Guo, W. Ji, and D. Zhong, "Single-layer CrI_3 grown by molecular beam epitaxy," Sci. Bull. **65**, 1064–1071 (2020).
[165]D. J. O'Hara, T. Zhu, A. H. Trout, A. S. Ahmed, Y. K. Luo, C. H. Lee, M. R. Brenner, S. Rajan, J. A. Gupta, D. W. McComb, and R. K. Kawakami, "Room temperature intrinsic ferromagnetism in epitaxial manganese selenide films in the monolayer limit," Nano Lett. **18**, 3125–3131 (2018).
[166]P. M. Coelho, K. Nguyen Cong, M. Bonilla, S. Kolekar, M.-H. Phan, J. Avila, M. C. Asensio, I. I. Oleynik, and M. Batzill, "Charge density wave state suppresses ferromagnetic ordering in VSe_2 monolayers," J. Phys. Chem. C **123**, 14089–14096 (2019).
[167]A. O. Fumega, M. Gobbi, P. Dreher, W. Wan, C. González-Orellana, M. Peña-Díaz, C. Rogero, J. Herrero-Martín, P. Gargiani, M. Ilyn, M. M. Ugeda, V. Pardo, and S. Blanco-Canosa, "Absence of ferromagnetism in VSe_2 caused by its charge density wave phase," J. Phys. Chem. C **123**, 27802–27810 (2019).
[168]G. Schmidt, D. Ferrand, L. W. Molenkamp, A. T. Filip, and B. J. van Wees, "Fundamental obstacle for electrical spin injection from a ferromagnetic metal into a diffusive semiconductor," Phys. Rev. B **62**, R4790–R4793 (2000).
[169]E. I. Rashba, "Theory of electrical spin injection: Tunnel contacts as a solution of the conductivity mismatch problem," Phys. Rev. B **62**, R16267–R16270 (2000).
[170]W. Zhang, J. Sklenar, B. Hsu, W. Jiang, M. B. Jungfleisch, J. Xiao, F. Y. Fradin, Y. Liu, J. E. Pearson, J. B. Ketterson, Z. Yang, and A. Hoffmann, "Research Update: Spin transfer torques in permalloy on monolayer MoS_2," APL Mater. **4**, 032302 (2016).
[171]K. Kondou, R. Yoshimi, A. Tsukazaki, Y. Fukuma, J. Matsuno, K. S. Takahashi, M. Kawasaki, Y. Tokura, and Y. Otani, "Fermi-level-dependent charge-to-spin current conversion by Dirac surface states of topological insulators," Nat. Phys. **12**, 1027–1031 (2016).
[172]F. Bonell, M. Goto, G. Sauthier, J. F. Sierra, A. I. Figueroa, M. V. Costache, S. Miwa, Y. Suzuki, and S. O. Valenzuela, "Control of spin–orbit torques by interface engineering in topological insulator heterostructures," Nano Lett. **20**, 5893–5899 (2020).
[173]X. Wang, J. Tang, X. Xia, C. He, J. Zhang, Y. Liu, C. Wan, C. Fang, C. Guo, W. Yang, Y. Guang, X. Zhang, H. Xu, J. Wei, M. Liao, X. Lu, J. Feng, X. Li, Y. Peng, H. Wei, R. Yang, D. Shi, X. Zhang, Z. Han, Z. Zhang, G. Zhang, G. Yu, and X. Han, "Current-driven magnetization switching in a van der Waals ferromagnet Fe_3GeTe_2," Sci. Adv. **5**, eaaw8904 (2019).
[174]V. Gupta, T. M. Cham, G. M. Stiehl, A. Bose, J. A. Mittelstaedt, K. Kang, S. Jiang, K. F. Mak, J. Shan, R. A. Buhrman, and D. C. Ralph, "Manipulation of the van der Waals magnet $Cr_2Ge_2Te_6$ by spin–orbit torques," Nano Lett. **20**, 7482–7488 (2020).
[175]M. Alghamdi, M. Lohmann, J. Li, P. R. Jothi, Q. Shao, M. Aldosary, T. Su, B. P. T. Fokwa, and J. Shi, "Highly efficient spin–orbit torque and switching of layered ferromagnet Fe_3GeTe_2," Nano Lett. **19**, 4400–4405 (2019).
[176]V. Ostwal, T. Shen, and J. Appenzeller, "Efficient spin-orbit torque switching of the semiconducting van der Waals ferromagnet $Cr_2Ge_2Te_6$," Adv. Mater. **32**, 1906021 (2020).
[177]Y. Fan, P. Upadhyaya, X. Kou, M. Lang, S. Takei, Z. Wang, J. Tang, L. He, L.-T. Chang, M. Montazeri, G. Yu, W. Jiang, T. Nie, R. N. Schwartz, Y. Tserkovnyak, and K. L. Wang, "Magnetization switching through giant spin–orbit torque in a magnetically doped topological insulator heterostructure," Nat. Mater. **13**, 699–704 (2014).
[178]I. Shin, W. J. Cho, E.-S. An, S. Park, H.-W. Jeong, S. Jang, W. J. Baek, S. Y. Park, D.-H. Yang, J. H. Seo, G.-Y. Kim, M. N. Ali, S.-Y. Choi, H.-W. Lee, J. S. Kim, S. Kim, and G.-H. Lee, "Spin-orbit torque switching in an all-van der Waals heterostructure," arXiv:2102.09300 (2021).
[179]M. Gmitra and J. Fabian, "Graphene on transition-metal dichalcogenides: A platform for proximity spin-orbit physics and optospintronics," Phys. Rev. B **92**, 155403 (2015).
[180]M. Morota, Y. Niimi, K. Ohnishi, D. H. Wei, T. Tanaka, H. Kontani, T. Kimura, and Y. Otani, "Indication of intrinsic spin Hall effect in 4d and 5d transition metals," Phys. Rev. B **83**, 174405 (2011).
[181]L. Vila, T. Kimura, and Y. Otani, "Evolution of the spin Hall effect in Pt nanowires: Size and temperature effects," Phys. Rev. Lett. **99**, 226604 (2007).
[182]E. Sagasta, Y. Omori, M. Isasa, M. Gradhand, L. E. Hueso, Y. Niimi, Y. Otani, and F. Casanova, "Tuning the spin Hall effect of Pt from the moderately dirty to the superclean regime," Phys. Rev. B **94**, 060412(R) (2016).
[183]C. K. Safeer, J. Ingla-Aynés, N. Ontoso, F. Herling, W. Yan, L. E. Hueso, and F. Casanova, "Spin Hall effect in bilayer graphene combined with an insulator up to room temperature," Nano Lett. **20**(6), 4573–4579 (2020).
[184]W. Savero Torres, J. F. Sierra, L. A. Benítez, F. Bonell, M. V. Costache, and S. O. Valenzuela, "Spin precession and spin Hall effect in monolayer graphene/Pt nanostructures," 2D Mater. **4**, 041008 (2017).
[185]W. Yan, E. Sagasta, M. Ribeiro, Y. Niimi, L. E. Hueso, and F. Casanova, "Large room temperature spin-to-charge conversion signals in a few-layer graphene/Pt lateral heterostructure," Nat. Commun. **8**, 661 (2017).
[186]C. K. Safeer, J. Ingla-Aynés, F. Herling, J. H. Garcia, M. Vila, N. Ontoso, M. R. Calvo, S. Roche, L. E. Hueso, and F. Casanova, "Room-temperature spin Hall effect in graphene/MoS_2 van der Waals heterostructures," Nano Lett. **19**, 1074–1082 (2019).
[187]L. A. Benítez, W. Savero Torres, J. F. Sierra, M. Timmermans, J. H. Garcia, S. Roche, M. V. Costache, and S. O. Valenzuela, "Tunable room-temperature spin galvanic and spin Hall effects in van der Waals heterostructures," Nat. Mater. **19**, 170–175 (2020).
[188]T. S. Ghiasi, A. A. Kaverzin, P. J. Blah, and B. J. Van Wees, "Charge-to-spin conversion by the Rashba–Edelstein effect in two-dimensional van der Waals heterostructures up to room temperature," Nano Lett. **19**(9), 5959–5966 (2019).
[189]F. Herling, C. K. Safeer, J. Ingla-Aynés, N. Ontoso, L. E. Hueso, and F. Casanova, "Gate tunability of highly efficient spin-to-charge conversion by spin Hall effect in graphene proximitized with WSe_2," APL Mater. **8**, 071103 (2020).
[190]L. Li, J. Zhang, G. Myeong, W. Shin, H. Lim, B. Kim, S. Kim, T. Jin, S. Cavill, B. S. Kim, C. Kim, J. Lischner, A. Ferreira, and S. Cho, "Gate-tunable reversible Rashba–Edelstein effect in a few-layer graphene/2H-TaS_2 heterostructure at room temperature," ACS Nano **14**(5), 5251–5259 (2020).
[191]D. Khokhriakov, A. M. Hoque, B. Karpiak, and S. P. Dash, "Gate-tunable spin-galvanic effect in graphene-topological insulator van der Waals heterostructures at room temperature," Nat. Commun. **11**, 3657 (2020).
[192]C. K. Safeer, N. Ontoso, J. Ingla-Aynés, F. Herling, V. T. Pham, A. Kurzmann, K. Ensslin, A. Chuvilin, I. Robredo, M. G. Vergniory, F. de Juan, L. E. Hueso, M. R. Calvo, and F. Casanova, "Large multidirectional spin-to-charge conversion in low-symmetry semimetal $MoTe_2$ at room temperature," Nano Lett. **19**, 8758–8766 (2019).
[193]B. Zhao, B. Karpiak, D. Khokhriakov, A. Johansson, A. M. Hoque, X. Xu, Y. Jiang, I. Mertig, and S. P. Dash, "Unconventional charge-spin conversion in Weyl-semimetal WTe_2," Adv. Mater. **32**, 2000818 (2020).
[194]K. Garello, I. M. Miron, C. O. Avci, F. Freimuth, Y. Mokrousov, S. Blügel, S. Auffret, O. Boulle, G. Gaudin, and P. Gambardella, "Symmetry and magnitude

of spin-orbit torques in ferromagnetic heterostructures," Nat. Nanotechnol. **8**, 587–593 (2013).
[195]Y. Tserkovnyak, A. Brataas, and G. E. W. Bauer, "Enhanced Gilbert damping in thin ferromagnetic films," Phys. Rev. Lett. **88**, 117601 (2002).
[196]Y. Fan, X. Kou, P. Upadhyaya, Q. Shao, L. Pan, M. Lang, X. Che, J. Tang, M. Montazeri, K. Murata, L.-T. Chang, M. Akyol, G. Yu, T. Nie, K. L. Wong, J. Liu, Y. Wang, Y. Tserkovnyak, and K. L. Wang, "Electric-field control of spin-orbit torque in a magnetically doped topological insulator," Nat. Nanotechnol. **11**, 352–359 (2016).
[197]K. Yasuda, A. Tsukazaki, R. Yoshimi, K. Kondou, K. S. Takahashi, Y. Otani, M. Kawasaki, and Y. Tokura, "Current-nonlinear Hall effect and spin-orbit torque magnetization switching in a magnetic topological insulator," Phys. Rev. Lett. **119**, 137204 (2017).
[198]J. B. S. Mendes, O. Alves Santos, J. Holanda, R. P. Loreto, C. I. L. de Araujo, C.-Z. Chang, J. S. Moodera, A. Azevedo, and S. M. Rezende, "Dirac-surface-state-dominated spin to charge current conversion in the topological insulator $(Bi_{0.22}Sb_{0.78})_2Te_3$ films at room temperature," Phys. Rev. B **96**, 180415 (2017).
[199]J. C. Rojas Sánchez, L. Vila, G. Desfonds, S. Gambarelli, J. P. Attané, J. M. De Teresa, C. Magén, and A. Fert, "Spin-to-charge conversion using Rashba coupling at the interface between non-magnetic materials," Nat. Commun. **4**, 2944 (2013).
[200]J.-C. Rojas-Sánchez, S. Oyarzún, Y. Fu, A. Marty, C. Vergnaud, S. Gambarelli, L. Vila, M. Jamet, Y. Ohtsubo, A. Taleb-Ibrahimi, P. Le Fèvre, F. Bertran, N. Reyren, J.-M. George, and A. Fert, "Spin to charge conversion at room temperature by spin pumping into a new type of topological insulator: α-Sn films," Phys. Rev. Lett. **116**, 096602 (2016).
[201]J. Hidding and M. H. D. Guimarães, "Spin-orbit torques in transition metal dichalcogenide/ferromagnet heterostructures," Front. Mater. **7**, 594771 (2020).
[202]W. Lv, Z. Jia, B. Wang, Y. Lu, X. Luo, B. Zhang, Z. Zeng, and Z. Liu, "Electric-field control of spin-orbit torques in WS_2/permalloy bilayers," ACS Appl. Mater. Interfaces **10**, 2843–2849 (2018).
[203]D. MacNeill, G. M. Stiehl, M. H. D. Guimarães, N. D. Reynolds, R. A. Buhrman, and D. C. Ralph, "Thickness dependence of spin-orbit torques generated by WTe_2," Phys. Rev. B **96**, 054450 (2017).
[204]D. MacNeill, G. M. Stiehl, M. H. D. Guimaraes, R. A. Buhrman, J. Park, and D. C. Ralph, "Control of spin-orbit torques through crystal symmetry in WTe_2/ferromagnet bilayers," Nat. Phys. **13**(3), 300–305 (2017).
[205]P. Li, W. Wu, Y. Wen, C. Zhang, J. Zhang, S. Zhang, Z. Yu, S. A. Yang, A. Manchon, and X.-X. Zhang, "Spin-momentum locking and spin-orbit torques in magnetic nano-heterojunctions composed of Weyl semimetal WTe_2," Nat. Commun. **9**, 3990 (2018).
[206]S. Shi, S. Liang, Z. Zhu, K. Cai, S. D. Pollard, Y. Wang, J. Wang, Q. Wang, P. He, J. Yu, G. Eda, G. Liang, and H. Yang, "All-electric magnetization switching and Dzyaloshinskii–Moriya interaction in WTe_2/ferromagnet heterostructures," Nat. Nanotechnol. **14**(10), 945–949 (2019).
[207]J. B. S. Mendes, A. Aparecido-Ferreira, J. Holanda, A. Azevedo, and S. M. Rezende, "Efficient spin to charge current conversion in the 2D semiconductor MoS_2 by spin pumping from yttrium iron garnet," Appl. Phys. Lett. **112**, 242407 (2018).
[208]Ø. Johansen, V. Risinggård, A. Sudbø, J. Linder, and A. Brataas, "Current control of magnetism in two-dimensional Fe_3GeTe_2," Phys. Rev. Lett. **122**, 217203 (2019).
[209]S. Laref, K.-W. Kim, and A. Manchon, "Elusive Dzyaloshinskii–Moriya interaction in monolayer Fe_3GeTe_2," Phys. Rev. B **102**, 060402(R) (2020).
[210]K. Zhang, S. Han, Y. Lee, M. J. Coak, J. Kim, I. Hwang, S. Son, J. Shin, M. Lim, D. Jo, K. Kim, D. Kim, H. W. Lee, and J. G. Park, "Gigantic current control of coercive field and magnetic memory based on nanometer-thin ferromagnetic van der Waals Fe_3GeTe_2," Adv. Mater. **33**, 2004110 (2021).
[211]P. D. C. King, R. C. Hatch, M. Bianchi, R. Ovsyannikov, C. Lupulescu, G. Landolt, B. Slomski, J. H. Dil, D. Guan, J. L. Mi, E. D. L. Rienks, J. Fink, A. Lindblad, S. Svensson, S. Bao, G. Balakrishnan, B. B. Iversen, J. Osterwalder, W. Eberhardt, F. Baumberger, and P. Hofmann, "Large tunable Rashba spin splitting of a two-dimensional electron gas in Bi_2Se_3," Phys. Rev. Lett. **107**, 096802 (2011).
[212]J. Zhang, J. P. Velev, X. Dang, and E. Y. Tsymbal, "Band structure and spin texture of Bi_2Se_3 3d ferromagnetic metal interface," Phys. Rev. B **94**, 014435 (2016).
[213]J. M. Marmolejo-Tejada, K. Dolui, P. Lazić, P.-H. Chang, S. Smidstrup, D. Stradi, K. Stokbro, and B. K. Nikolić, "Proximity band structure and spin textures on both sides of topological-insulator/ferromagnetic-metal interface and their charge transport probes," Nano Lett. **17**, 5626–5633 (2017).
[214]L. A. Walsh, C. M. Smyth, A. T. Barton, Q. Wang, Z. Che, R. Yue, J. Kim, M. J. Kim, R. M. Wallace, and C. L. Hinkle, "Interface chemistry of contact metals and ferromagnets on the topological insulator Bi_2Se_3," J. Phys. Chem. C **121**(42), 23551–23563 (2017).
[215]J. Li, Z. Y. Wang, A. Tan, P.-A. Glans, E. Arenholz, C. Hwang, J. Shi, and Z. Q. Qiu, "Magnetic dead layer at the interface between a Co film and the topological insulator Bi_2Se_3," Phys. Rev. B **86**(5), 054430 (2012).
[216]V. P. Amin, P. M. Haney, and M. D. Stiles, "Interfacial spin-orbit torques," J. Appl. Phys. **128**, 151101 (2020).
[217]K. M. D. Hals and A. Brataas, "Phenomenology of current-induced spin-orbit torques," Phys. Rev. B **88**, 085423 (2013).
[218]M. Seemann, D. Ködderitzsch, S. Wimmer, and H. Ebert, "Symmetry-imposed shape of linear response tensors," Phys. Rev. B **92**, 155138 (2015).
[219]Y. C. Cheng, Z. Y. Zhu, M. Tahir, and U. Schwingenschlögl, "Spin-orbit-induced spin splittings in polar transition metal dichalcogenide monolayers," Europhys. Lett. **102**, 57001 (2013).
[220]M. Gmitra, D. Kochan, P. Högl, and J. Fabian, "Trivial and inverted Dirac bands and the emergence of quantum spin Hall states in graphene on transition-metal dichalcogenides," Phys. Rev. B **93**, 155104 (2016).
[221]J. H. Garcia, M. Vila, A. W. Cummings, and S. Roche, "Spin transport in graphene/transition metal dichalcogenide heterostructures," Chem. Soc. Rev. **47**, 3359–3379 (2018).
[222]J. H. Garcia, M. Vila, C.-H. Hsu, X. Waintal, V. M. Pereira, and S. Roche, "Canted persistent spin texture and quantum spin Hall effect in WTe_2," Phys. Rev. Lett. **125**, 256603 (2020).
[223]Q. Wu, S. Zhang, H.-F. Song, M. Troyer, and A. A. Soluyanov, "WannierTools: An open-source software package for novel topological materials," Comput. Phys. Commun. **224**, 405–416 (2018).
[224]I. Smaili, S. Laref, J. H. Garcia, U. Schwingenschlögl, S. Roche, and A. Manchon, "Janus monolayers of magnetic transition metal dichalcogenides as an all-in-one platform for spin-orbit torque," Phys. Rev. B **104**, 104415 (2021).
[225]Z. Fan, J. H. Garcia, A. W. Cummings, J. E. Barrios-Vargas, M. Panhans, A. Harju, F. Ortman, and S. Roche, "Linear scaling quantum transport methodologies," Phys. Rep. **903**, 1–69 (2020).
[226]J. H. Garcia, A. W. Cummings, and S. Roche, "Spin Hall effect and weak antilocalization in graphene/transition metal dichalcogenide heterostructures," Nano Lett. **17**, 5078–5083 (2017).
[227]M. Offidani, M. Milletarì, R. Raimondi, and A. Ferreira, "Optimal charge-to-spin conversion in graphene on transition-metal dichalcogenides," Phys. Rev. Lett. **119**, 196801 (2017).
[228]H. Li, X. Wang, and A. Manchon, "Valley-dependent spin-orbit torques in two-dimensional hexagonal crystals," Phys. Rev. B **93**, 035417 (2016).
[229]L. Liu, C. Zhou, X. Shu, C. Li, T. Zhao, W. Lin, J. Deng, Q. Xie, S. Chen, J. Zhou, R. Guo, H. Wang, J. Yu, S. Shi, P. Yang, S. Pennycook, A. Manchon, and J. Chen, "Symmetry-dependent field-free switching of perpendicular magnetization," Nat. Nanotechnol. **16**, 277–282 (2021).
[230]Z. Zhang, X. Ni, H. Huang, L. Hu, and F. Liu, "Valley splitting in the van der Waals heterostructure WSe_2/CrI_3: The role of atom superposition," Phys. Rev. B **99**, 115441 (2019).
[231]T. Hu, G. Zhao, H. Gao, Y. Wu, J. Hong, A. Stroppa, and W. Ren, "Manipulation of valley pseudospin in WSe_2/CrI_3 heterostructures by the magnetic proximity effect," Phys. Rev. B **101**, 125401 (2020).
[232]D. Zhong, K. L. Seyler, X. Linpeng, N. P. Wilson, T. Taniguchi, K. Watanabe, M. A. McGuire, K.-M. C. Fu, D. Xiao, W. Yao, and X. Xu, "Layer-resolved magnetic proximity effect in van der Waals heterostructures," Nat. Nanotechnol. **15**, 187–191 (2020).
[233]S. Shi, A. Wang, Y. Wang, R. Ramaswamy, L. Shen, J. Moon, D. Zhu, J. Yu, S. Oh, Y. Feng, and H. Yang, "Efficient charge-spin conversion and magnetization

switching through the Rashba effect at topological-insulator/Ag interfaces," Phys. Rev. B **97**, 041115 (2018).
[234]P. Deorani, J. Son, K. Banerjee, N. Koirala, M. Brahlek, S. Oh, and H. Yang, "Observation of inverse spin Hall effect in bismuth selenide," Phys. Rev. B **90**, 094403 (2014).
[235]M. Jamali, J. S. Lee, J. S. Jeong, F. Mahfouzi, Y. Lv, Z. Zhao, B. K. Nikolić, K. A. Mkhoyan, N. Samarth, and J.-P. Wang, "Giant spin pumping and inverse spin Hall effect in the presence of surface and bulk spin-orbit coupling of topological insulator Bi_2Se_3," Nano Lett. **15**(10), 7126–7132 (2015).
[236]T. Guillet, C. Zucchetti, A. Marchionni, A. Hallal, P. Biagioni, C. Vergnaud, A. Marty, H. Okuno, A. Masseboeuf, M. Finazzi, F. Ciccacci, M. Chshiev, F. Bottegoni, and M. Jamet, "Spin orbitronics at a topological insulator-semiconductor interface," Phys. Rev. B **101**, 184406 (2020).
[237]H. Wang, J. Kally, J. S. Lee, T. Liu, H. Chang, D. Reifsnyder Hickey, K. A. Mkhoyan, M. Wu, A. Richardella, and N. Samarth, "Surface-state-dominated spin-charge current conversion in topological-insulator–ferromagnetic-insulator heterostructures," Phys. Rev. Lett. **117**, 076601 (2016).
[238]Z. Zheng, Y. Zhang, D. Zhu, K. Zhang, X. Feng, Y. He, L. Chen, Z. Zhang, D. Liu, Y. Zhang, P. K. Amiri, and W. Zhao, "Perpendicular magnetization switching by large spin-orbit torques from sputtered Bi_2Te_3," Chin. Phys. B **29**, 078505 (2020).
[239]G. M. Stiehl, D. MacNeill, N. Sivadas, I. El Baggari, M. H. D. Guimarães, N. D. Reynolds, L. F. Kourkoutis, C. J. Fennie, R. A. Buhrman, and D. C. Ralph, "Current-induced torques with Dresselhaus symmetry due to resistance anisotropy in 2D materials," ACS Nano **13**, 2599–2605 (2019).
[240]G. M. Stiehl, R. Li, V. Gupta, I. El Baggari, S. Jiang, H. Xie, L. F. Kourkoutis, K. F. Mak, J. Shan, R. A. Buhrman, and D. C. Ralph, Phys. Rev. B **100**, 184402 (2019).
[241]H. Xu, J. Wei, H. Zhou, J. Feng, T. Xu, H. Du, C. He, Y. Huang, J. Zhang, Y. Liu, H.-C. Wu, C. Guo, X. Wang, Y. Guang, H. Wei, Y. Peng, W. Jiang, G. Yu, and X. Han, "High spin Hall conductivity in large-area type-II Dirac semimetal $PtTe_2$," Adv. Mater. **32**, 2000513 (2020).
[242]M. H. D. Guimarães, G. M. Stiehl, D. MacNeill, N. D. Reynolds, and D. C. Ralph, "Spin-orbit torques in $NbSe_2$/permalloy bilayers," Nano Lett. **18**, 1311–1316 (2018).
[243]S. Husain, X. Chen, R. Gupta, N. Behera, P. Kumar, T. Edvinsson, F. García-Sánchez, R. Brucas, S. Chaudhary, B. Sanyal, P. Svedlindh, and A. Kumar, "Large damping-like spin-orbit torque in a 2D conductive 1T-TaS_2 monolayer," Nano Lett. **20**, 6372–6380 (2020).
[244]C.-W. Peng, W.-B. Liao, T.-Y. Chen, and C.-F. Pai, "Efficient spin-orbit torque generation in semiconducting WTe_2 with hopping transport," ACS Appl. Mater. Interfaces **13**, 15950–15957 (2021).